University of Leoben

Role of microstructure on the electro-mechanical behaviour of copper films on polyimide

Diploma Thesis

by

Julia Berger

Leoben, May 2014

This work has been carried out at the Erich Schmid Institute of Materials Science with support for research provided by Austrian Science Foundation (FWF) through project: P22648-N20.

Erich Schmid Institute of Materials Science
Austrian Academy of Sciences
Jahnstraße 12
8700 Leoben
Austria

University of Leoben
Franz Josef Straße 18
8700 Leoben
Austria

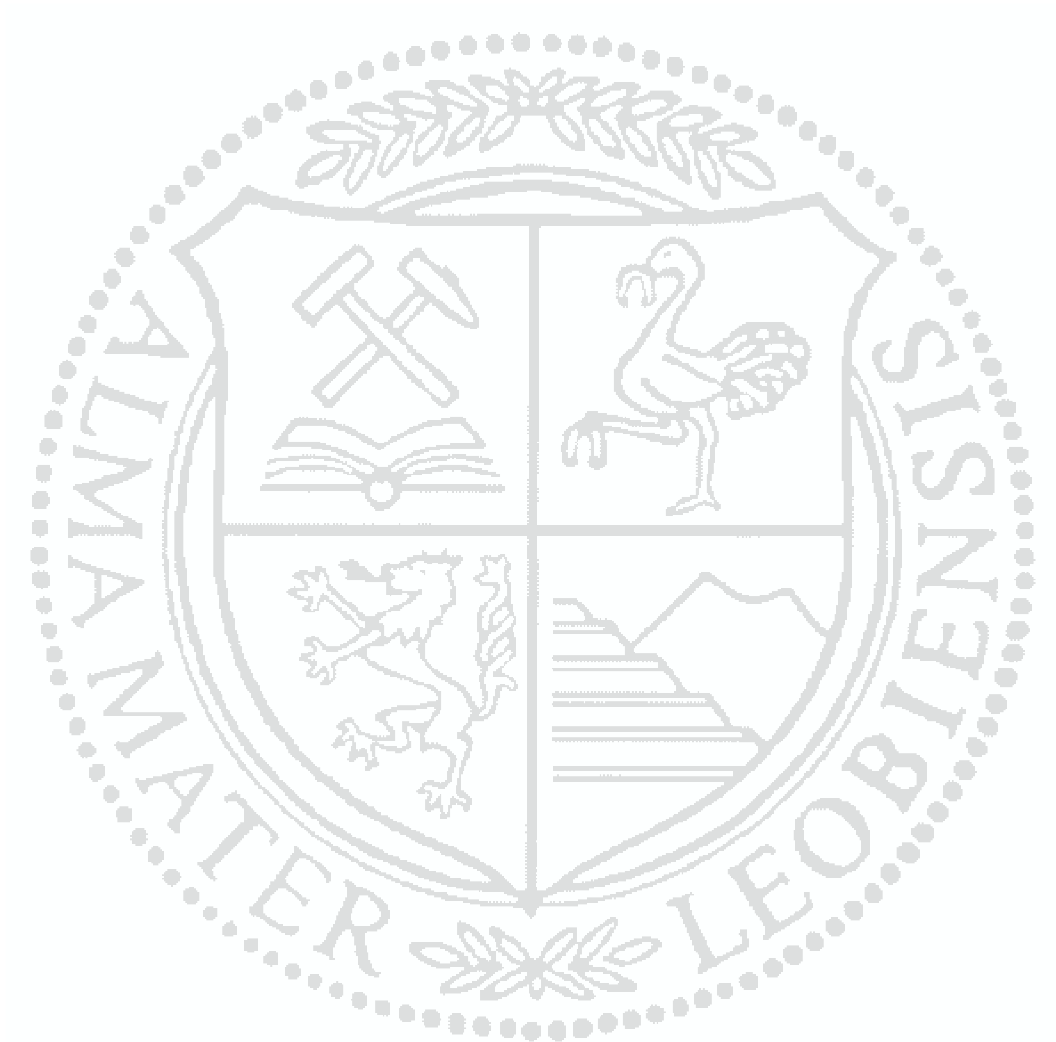

Affidavit

I declare in lieu of oath, that I wrote this thesis and performed the associated research myself, using only literature cited in this volume.

Leoben, Mai 2014

(Julia Berger)

i Acknowledgements

My sincere appreciation is due to my supervisor Dr. Megan Cordill for her guidance and encouragement over the last years, for all the knowledge she was able to impart to me and for supporting me far beyond my diploma thesis.

I would like to express my gratitude to Dr. Oleksandr Glushko for introducing me into most of the experimental tools needed for my thesis and lending a helping hand whenever needed.

Furthermore, I am very grateful to Dr. Thomas Schöberl, an expert on handling our pretty old atomic force microscope, for knowing exactly “how to pander to the machine’s whims” and thus helping me to save time and nerves implementing my experiments.

For the technical support I would like to thank the team of the workshop, especially Franz Hubner, for constructing the screw-driven tensile straining device needed for executing the in-situ tensile tests. Moreover thanks to Viktoria Schrutt and Maria Fließer for their organisational support.

Many special thanks to all my colleagues of the Erich Schmid Institute for the good advice and for the great working atmosphere. I really enjoyed working with all of you! I particularly would like to give thanks to DI Bernhard Völker and DI Ruth Treml for the ion channelling contrast images, DI Karoline Karmout and Dr. Verena Maier for the transmission electron micrographs and DI Roland Kasberger, who spent so much time on introducing me into digital image correlation.

My deepest appreciation to my best friend Nikolaus Jäger for not giving up explaining me the same things again and again until I understood them. Without you, everything would have been far more difficult! I would also like to express my thankfulness to all those friends, who remain unnamed, but who have also made their contribution to my achievements. Thanks for making these years of study unforgettable for me!

I would like to thank my parents and grandparents not only for their financial support, also for their continuous love, for believing in me and encouraging me whenever I needed it the most. Moreover, thanks to my sister for always having a sympathetic ear and for reminding me, not to take everything too seriously.

Finally, I want to express my gratitude to Florian for his ability to calm me down and to make me smile and for encouraging and supporting me in all my decisions.

ii Abstract

Metal films on flexible polymer substrates are commonly used in flexible electronic devices and may be exposed to repeated large deformations during manufacturing and application. To ensure a long life time of flexible electronics, these compound systems have to be robust and reliable while stretching and compressing without failing mechanically or electrically. The goal of this work was to examine the influence of microstructure and film thickness on the electro-mechanical deformation behaviour of copper-polymer film-substrate systems. Therefore, four different copper films on 50 µm polyimide substrates with variation in thickness (50 nm, 100 nm and 200 nm) and grain size due to annealing were tested.

The microstructure of the Cu films was determined using electron backscatter diffraction, focused ion beam and transmission electron microscopy. The choice of method depended on the thickness of the investigated film. The average grain size was found to be approximately in the range of the film thickness. The 50 nm and the 100 nm thick films only possessed nano-sized grains, the as-deposited and annealed 200 nm thick Cu films exhibited large micron-sized grains.

The deformation behaviour of the substrate bonded Cu films was determined by in-situ tensile tests, both mechanically with fragmentation tests under the atomic force microscope and electrically with 4 point probe resistance measurements. The onset of plastic deformation in the form of localized thinning at the surface was detected at low strains for all film thicknesses, whereas for films with coarser grains and larger film thicknesses necks formed earlier. Although the deformation density rose with increasing strain for all samples, the electrical conductivity of the Cu films did not deteriorate exceedingly for the 100 nm and 200 nm films. The 50 nm films, however, showed a great deterioration of the conductivity due to the formation of cracks.

In conclusion, Cu films with a film thickness under 100 nm showed a rather brittle deformation behaviour caused by their nano-sized grains. Above 100 nm film thickness ductile deformation behaviour was observed. Instead of cracks only necks formed in the film during straining, which could be attributed to the presence of large grains in the range of microns.

iii Kurzfassung

Auf Kunststoffsubstrat abgeschiedene Metallfilme finden häufig Einsatz in flexiblen elektronischen Geräten und werden während Produktion und Anwendung wiederholt enormen Verformungen ausgesetzt. Um eine möglichst lange Lebensdauer dieser Bauteile gewährleisten zu können, müssen diese Verbundsysteme robust und zuverlässig bei Dehnung und Stauchung sein, ohne mechanisch oder elektrisch zu versagen. Ziel dieser Arbeit war es, einen tieferen Einblick in das elektromechanische Verformungsverhalten von Kupfer-Kunststoff-Verbunden zu erlangen und festzustellen, in wie fern Variationen bezüglich Schichtdicke und Mikrostruktur sowie zusätzliche Glühbehandlungen das Deformationsverhalten der Metallschichten beeinflussen. Hierfür wurden auf 50 µm dickes Polyimidsubstrat aufgedampfte Kupferschichten mit unterschiedlichen Schichtdicken (50 nm, 100 nm und 200 nm) und Korngrößen untersucht.

Abhängig von der Schichtdicke des Metallfilms wurde das Gefüge der Kupferdünnschichten mittels Elektronenrückstrahlbeugung, mit fokussiertem Ionenstrahl oder mit Hilfe des Transmissionselektronenmikroskops bestimmt. Die durchschnittliche Korngröße lag hierbei in der Größenordnung der Schichtdicke. 200 nm dicke Kupferschichten wiesen zusätzlich zu ihrer im Nanometerbereich liegenden Matrix µm-große Körner auf.

Das Deformationsverhalten der Kupfer-Kunststoff-Verbunde wurde mittels in-situ Zugversuchen mechanischer (mittels Fragmentierungstest) und elektrischer Natur (mittels 4-Punkt-Widerstandsmessung) untersucht. Erste Zeichen plastischer Verformung in Form von lokaler Querschnittsabnahme der Metallschicht (Einschnürung) wurden bereits bei niedrigen Dehnungen bei allen Schichtdicken entdeckt. Diese Einschnürungen bildeten sich umso früher aus, je größer Schichtdicken und Körner der Kupferfilme waren. Obwohl die Dichte derartiger Verformungen mit zunehmender Dehnung anstieg, verschlechterte sich die elektrische Leitfähigkeit der 100 nm und 200 nm dicken Kupferschichten nicht übermäßig. Bei den 50 nm dicken Schichten hingegen bildeten sich während des Dehnens Risse im Cu-Film, welche zu einer enormen Verschlechterung der elektrischen Leitfähigkeit führten.

Kupferfilme mit Schichtdicken $<$ 100 nm neigten aufgrund ihres nanokristallinen Gefüges zu spröder Verformung, welche sich in Form von Rissbildung veranschaulichte. Bei Schichtdicken $>$ 100 nm wurde ein duktiles Deformationsverhalten beobachtet. Anstelle der Risse bildeten sich während der Zugbeanspruchung lediglich Einschnürungen im Kupferfilm aus, wobei dieses Verhalten auf die vorhandenen µm-großen Körner zurückgeführt wurde.

Contents

i Acknowledgements .... **i**

ii Abstract .... **ii**

iii Kurzfassung .... **iii**

1 Motivation **1**

2 Literature overview **2**

2.1 Introduction 2

2.2 Fragmentation testing 2

2.3 In-situ resistance measurements 6

2.4 Deformation behaviour of metal films on compliant substrates 9

2.4.1 Shear lag theory for brittle metal films 9

2.4.2 Ductile metal films 11

2.4.3 Effects on the deformation behaviour of thin film systems 12

3 Experimental **17**

3.1 Film deposition 17

3.2 Microstructure determination 17

3.2.1 200 nm thick copper films on polyimide 17

3.2.2 Copper films with film thicknesses below 200 nm 18

3.3 In-situ fragmentation testing under the AFM 18

3.3.1 Test execution 18

3.3.2 Analysis 19

3.4 In-situ resistance measurements 23

3.5 In-situ EBSD tensile tests 25

3.6 Post-mortem determination 25

4 Microstructure characterization **26**

5 **Fragmentation testing under the AFM** **32**

5.1 Effect of film thickness 32

5.2 Effect of microstructure 34

5.3 Drawbacks of the AFM fragmentation test method 36

5.4 Summary 37

6 **In-situ resistance measurements** **38**

6.1 Determination of R_{const} 38

6.2 Effect of film thickness 38

6.3 Effect of microstructure 40

6.4 Summary 42

7 **Conclusion** **43**

List of abbreviations .... **iv**

List of figures .... **vii**

List of tables .... **xi**

References .... **xii**

1 Motivation

Metal films on polymer substrates are commonly used in flexible electronic devices and may be exposed to repeated large deformations during manufacturing and application. Hence, for flexible electronics the main requirements of metal films on polymer substrates are to be very robust and reliable while stretching and compressing without failing mechanically or electrically.

Therefore, the deformation behaviour of thin Cu films on polyimide (PI) has been studied in this thesis by executing in-situ straining experiments under the atomic force microscope in order to detect first signs of plastic deformation in the form of localized thinning. The failure strains of the films have been determined with this method. Besides the visible detection of the failure strain, in-situ 4-point probe resistance fragmentation testing has also been performed. Both fragmentation testing methods have been executed for four different copper films on PI varying in film thickness and microstructure. Thus, microstructural investigations also show a correlation between grain size and deformation behaviour.

An important requirement for the utilisation in microelectronics is a good thermal fatigue resistance of the substrate bonded films. So it has been further examined, if annealing of the 200 nm films does have an impact on the failure strains and on the electrical conductivity. In addition to this, in-situ tensile tests have been performed inside a scanning electron microscope making electron back scatter diffraction (EBSD) scans for the as-deposited and annealed 200 nm thick films. Grain sizes and orientations can be determined from the EBSD data at each straining step and the influence of straining on the microstructure was determined with the aid of all these tests. With the aid of all these tests, the influence of the film's microstructure on the electro-mechanical deformation behaviour of substrate bonded Cu films can be examined.

2 Literature overview

2.1 Introduction

Today, a main field of application for thin films on polymer substrates are flexible electronics. Flexible electronics have been developed for various applications, including paper-like electronic displays, rollable solar cells, smart electronic textiles, etc., pursuing the aims of light weight, low cost, large area, and robustness for electronic devices. The systems may be exposed to repeated large deformation during manufacturing and usage. While the polymer substrates can easily recover from large deformations, thin metal or ceramic films often fail at low strains. Hence, for flexible electronics the main requirements of metal films on polymer substrates are to be robust and reliable while stretching and compressing without failing mechanically or electrically. For optimal combined electro-mechanical properties, good adhesion and high fracture strains (i.e. strains, where first cracks appear) are needed [1,2]. Thus, understanding the deformation behaviour of thin films on compliant substrates is crucial for improving the lifetime of such electronic devices.

2.2 Fragmentation testing

A common methodology to measure the fracture and adhesion properties of metal or ceramic films on polymer substrates is the fragmentation test. The method has its origin in the determination of interfacial shear forces in fibre composite materials [3] and has been modified to apply to film-substrate-interfaces [4-6]. The fragmentation test makes it possible to observe cracking and delamination events in-situ while straining a film-substrate system under an optical microscope (OM), inside a scanning electron microscope (SEM) or under an atomic force microscope (AFM) under tension [7,8].

The fragmentation technique works fairly well for brittle metals, such as Cr, Ta or Ti, and ceramic films on compliant substrates. During a fragmentation experiment, channel cracks, also called through thickness cracks (TTCs), form perpendicular to the straining direction at low strains and at higher strains buckles (delamination of the film from the substrate) can arise transverse to the straining direction. The average crack spacing, which equals the averaged distance between two cracks, can be measured using OM, SEM or AFM micrographs and can then be plotted as a function of the applied strain as shown in Fig. 2.1a. The crack spacing can also be determined by taking several surface profiles across an entire micrograph and counting the number of cracks intersecting the line. The ratio between the

length of the surface profile, $l_{profile}$, and the number of cracks, N_{cracks}, corresponds to the crack spacing, λ_{crack}, as well as to the reciprocal of the crack density, ρ_{crack} (Equation 1) [7,8].

$$\lambda_{crack} = \frac{l_{profile}}{N_{cracks}} = \frac{1}{\rho_{crack}} \quad (1)$$

The number of cracks increases during straining and, as a consequence, the crack spacing decreases until a saturation stage is reached. At this point, no further cracks form. The crack spacing reaches a minimum and remains constant, which is indicated by the plateau in Fig. 2.1a. This phenomenon is described in more detail by the shear lag theory in section 2.4.1. Based on the crack spacing at saturation, $\lambda_{sat.(crack)}$, the interfacial shear strength between film and substrate can be calculated using the following equation:

$$\tau_{IFSS} \propto \frac{h\,\sigma_f}{\lambda_{sat.(crack)}} \quad (2)$$

where τ_{IFSS} is the maximum shear stress sustained at the interface, h the film thickness and σ_f the fracture stress of the film. The fracture stress can be obtained by measuring the fracture strain with the aid of in-situ tensile tests and is consequentially calculated via the Hooke's Law:

$$\sigma_f = \varepsilon_f E \quad (3)$$

where ε_f is the observed fracture strain (the strain, where first cracks appear) and E is the elastic modulus of the film [9,10].

Ductile films, such as Ag, Au and Cu, deform plastically before cracks are formed. In this case, localized film thinning, called necking, is the first sign of yield and can hardly be observed with OM or SEM, as depicted in Fig. 2.1c and Fig. 2.1d. Alternatively, straining has been realized in-situ under an AFM to exploit its quantitative surface imaging technique. With the AFM, first indications of localized plastic deformation can be detected as a change in the surface height, as it is shown in the AFM height profiles of Fig. 2.2. To distinguish between TTCs and necks, the following criteria were established by Cordill and Marx [7] for ductile metal films, where h is the film thickness and Δ is the average deformation (neck or crack) depth:

$$\frac{\Delta}{h} \geq 0.15 \quad for\ TTCs \quad (4)$$

$$\frac{\Delta}{h} < 0.15 \quad for\ necks \quad (5)$$

If the calculated ratio, Δ/h, exceeds 15% the deformation is considered as crack, otherwise it is a neck. Additionally, it can be mentioned that at positions where necks initiate, TTCs can eventually form at higher strains, as it is evident in Fig. 2.2. Equal to brittle films, the deformation spacing (i.e. the spacing between two deformation sites (both necks and cracks)) can be determined, showing the same trend as in brittle films (Fig. 2.1c). The deformation spacing decreases with increasing strain and saturates above a certain strain limit [8].

Furthermore, AFM can be used to determine the adhesion energy by measuring the dimensions of the compression-induced buckles that arise during tensile straining of a metal film - substrate compound. At higher strains, after the saturation stage has been reached, compressive transverse stresses arise in the film fragments due to the difference in the Poisson's ratio between film and substrate. These compressive stresses cause progressive buckling and delamination of film fragments transverse to the tensile loading direction. AFM was used to image and measure the buckle dimensions (width and height) in order to determine the adhesion energy of the interface [10-12].

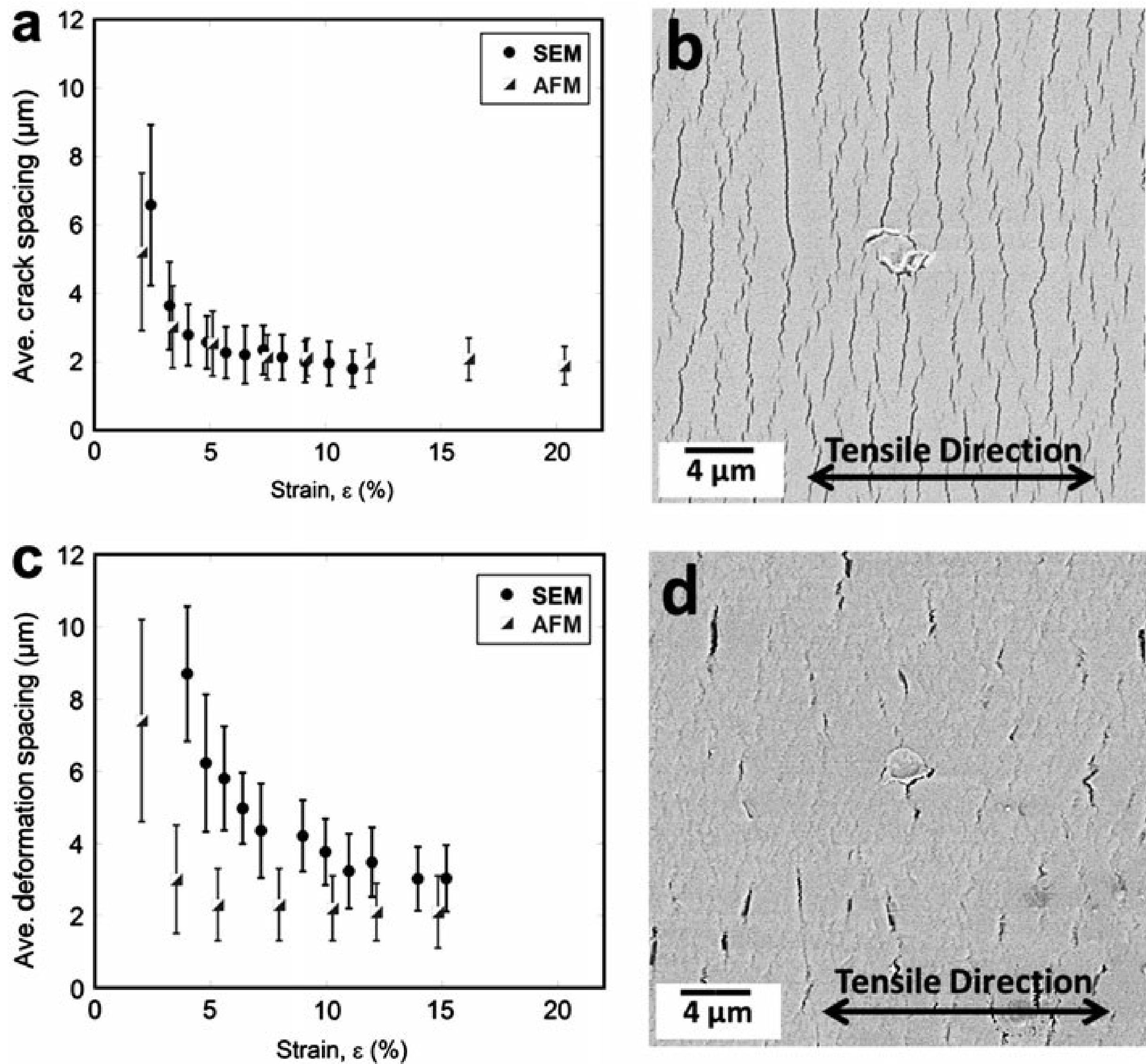

Fig. 2.1. *(a) Average (ave.) crack spacing as a function of strain of a 50 nm Cu/Cr film determined with the aid of AFM micrographs compared to the crack evolution established by SEM micrographs. (b) SEM micrograph at 20% strain of the 50 nm Cu/Cr film illustrating the brittle crack formation. (c) Change of the deformation spacings with increasing strain for a 200 nm Cu/Cr film. In contrast to (a), the deformation spacing determined with AFM and SEM micrographs have different values. This is because of the difficulty to accurately measure the TTC and neck spacings in SEM micrographs for ductile films, as demonstrated in (d) for a 15% strained, 200 nm Cu/Cr film. After a certain amount of strain, both films reach saturation in crack spacing (a) and deformation spacing (c), where no further cracks and necks form. This saturation is indicated by the plateau [8].*

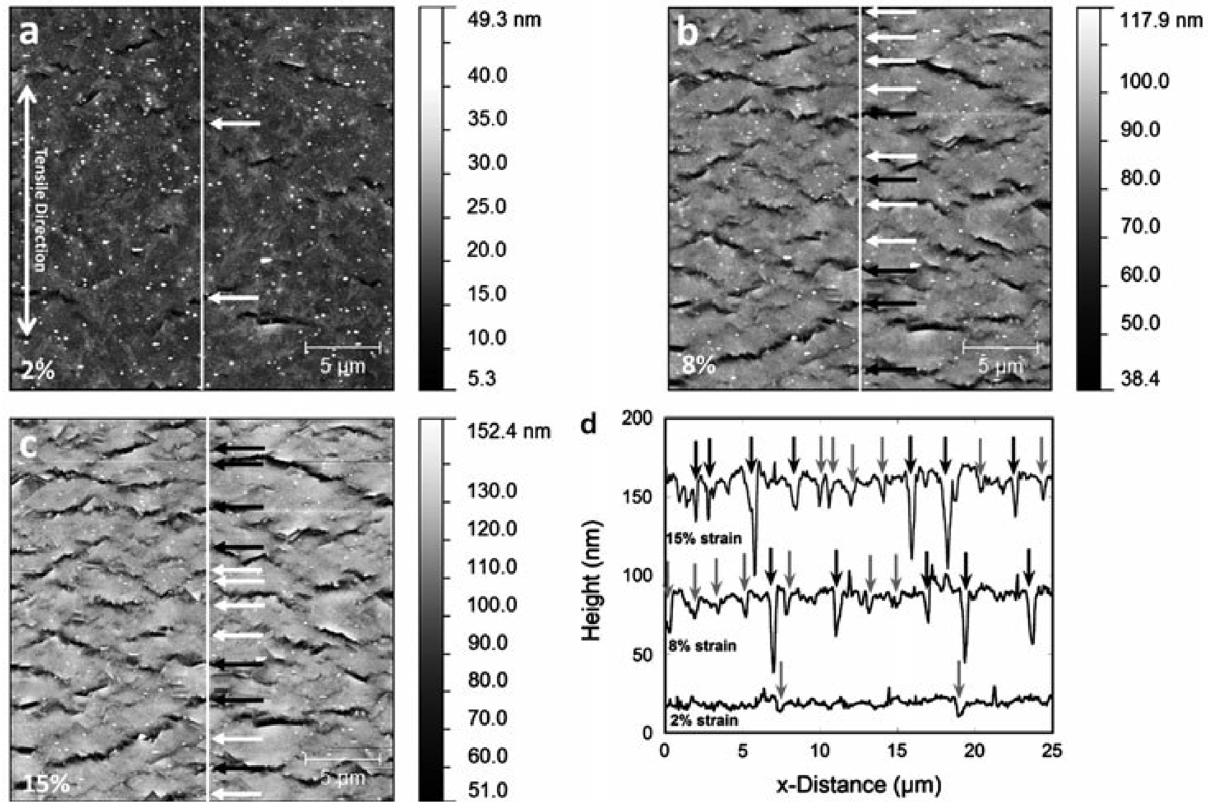

Fig. 2.2. AFM height images at (a) 2%, (b) 8% and (c) 15% strain of a 200 nm Cu/Cr/PI-system. In (d) the corresponding surface profiles from (a), (b) and (c) are shown and it is indicated where necks and TTCs have formed. Grey arrows represent necks and black arrows TCCs [8].

2.3 In-situ resistance measurements

Despite the large number of different mechanical phenomena which may appear in a film during straining like necking, cracking, buckling, etc., the electrical resistance of the film is one of the most important parameters regarding the functional stability of the metallization of flexible integrated circuits and is directly influenced by the formerly mentioned mechanical phenomena. If any mechanical damage is induced in the film, the electrical resistance of the film increases compared to its initial defect-free state. Measuring the alteration of the resistance of a metal film can therefore serve as a way to determine the presence of cracks. Strain-induced microstructural changes, such as the decrease of defect density or grain coarsening, might lead to a decrease of the electrical resistance, as reported by [13]. Moreover, film thickness and grain size also have an impact on the electrical properties, as it is discussed in more detail in Section 2.4. Thus, in-situ resistance measurements during tensile straining have been implemented by several groups for both monotonic and cyclic tensile testing on different metal-film/polymer-substrate systems (Cu-[14-18], Al-[19-21], Ag-[22]

film on PI- or polyethylene terephthalate (PET)- substrate), in order to understand how the deformation mechanisms and the electrical properties are related.

During straining the electrical resistance of a thin, conductive film is influenced by both, the change of the sample's geometry (i) and by structural modifications of the film (ii), e.g. the formation of necks, cracks, dislocation pile-ups, grain boundaries, point defects etc. Regarding (i), the resistance increases with tensile load due to the decreasing cross-section and the increasing length of the film [16].

Before straining in the ideal case of a uniform, homogeneous and defect-free film, the initial resistance, R_0, is given by Equation 6, where ρ is the resistivity, L_0 is the initial distance between the contacts, and A_0 is the initial cross-section of the film.

$$R_0 = \rho \frac{L_0}{A_0} \tag{6}$$

During straining, the instantaneous resistance, R, is defined by Equation 7, where the sample is stretched from L_0 for ΔL to the length, L, and the cross-section, A.

$$R = \rho \frac{L}{A} = \rho \frac{L_0 + \Delta L}{A} \tag{7}$$

Assuming that the electrical resistivity of the film does not change during plastic deformation of the film, the relative resistance, R/R_0, can be described by (8), taking into account that the volume of the film remains constant (A* L = A_0*L_0).

$$\frac{R}{R_0} = \left(\frac{L}{L_0}\right)^2 = (1+\varepsilon)^2 \tag{8}$$

However, when a film exhibits significant structural modifications (e.g. cracks), Equation 8 is no longer valid and the resistance curve varies from this theoretical prediction depending on film thickness and grain structure. As depicted in Fig. 2.3, the relative resistance (short dotted line) starts to deviate from Equation 8 (dashed line) at approximately 2-3% strain, when the transition from the linear to the non-linear regime of the stress strain curve takes place. In other words, the deviation from the theoretical curve starts at the beginning of plastic deformation of the sample [16].

To limit the relative resistance to the strained part of the sample for the implemented 4 point probe (4PP) resistance measurements, both R and R_0 have to be substituted by the contact resistance, R_{const}, which is the resistance of the film under the grips of the straining

device. In this part of the film no straining of the film occurs during the tensile test and therefore the resistance remains constant. The contact resistance is given by

$$R_{const} = R_{0meas} - R_{0samp} \qquad (9)$$

where R_{0meas} is the measured initial resistance in the straining device and R_{0samp} is the initial resistance of the sample, which has to be measured beforehand by a separate 4PP resistance measurement set-up. Thus, the relative resistance of the strained sample, R_{samp}/R_{0samp}, is given by (10) using Equation 9.

$$\frac{R_{samp}}{R_{0samp}} = \frac{R_{meas}}{R_{0meas}} + \frac{R_{const}}{R_{0samp}}\left(\frac{R_{meas}}{R_{0meas}} - 1\right) \qquad (10)$$

As a consequence, if the resistance is growing during straining, then

$$\frac{R_{samp}}{R_{0samp}} > \frac{R_{meas}}{R_{0meas}} \qquad (11)$$

i.e. the relative resistance of the strained part of the sample is always higher than the one measured by the ohmmeter. The parameter R_{const}/R_{0samp} defines how large this difference is. The deviation between the different curves, R_{samp}/R_{0samp} (red solid line), R/R_0 (short dotted line) and the theoretical prediction (dashed line), is shown in Fig. 2.3, where the relative resistance is plotted against the relative elongation for a 200 nm Cu/Cr/PET - system. If one ignores the contact resistance during straining, it leads to an underestimation of the resistance growth [16].

Moreover, as shown in Fig. 2.3, it is of prime importance to record both, the loading and the unloading curve of the straining experiment, because the resistance of the unloaded sample differs keenly from the one at maximum strain. This is due to the fact, that most of the cracks seen at the maximum strain are partially or fully closed when the sample is relaxed. Thus, in order to perform a correct coupled electro-mechanical analysis only the resistance after relaxation should be taken for comparison with post-mortem SEM micrographs [16]. The resistance recovery during un-loading of the sample is driven by two mechanisms: (i) the reverse change of the sample's geometry and (ii) the closure of small cracks as well as the bridging of larger ones. After the removal of the sample from the straining device, the sample macroscopically curls into a cylinder, so that the Cu film is facing outward. This is because the elastic strain of the polymer substrate is much higher than the one of the copper film and

therefore a compressive stress arises in the film during unloading. This compressive stress leads to re-connected cracks, which can facilitate new paths for the electric current [23].

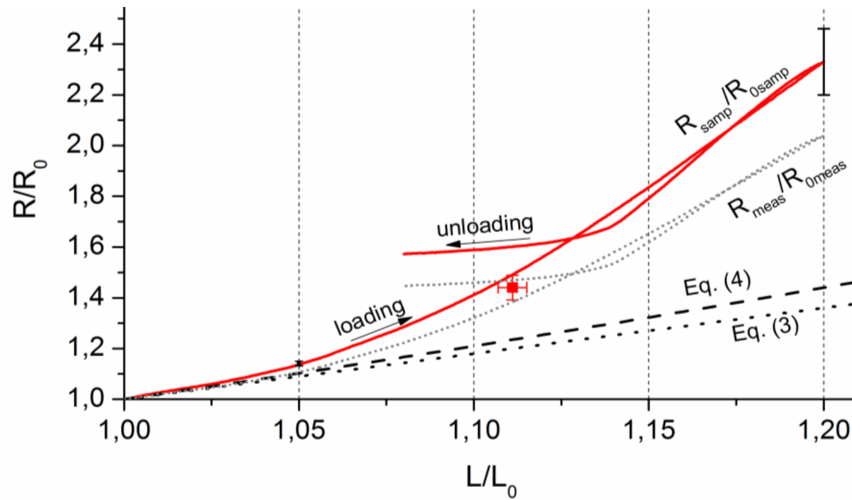

Fig. 2.3. *Change of the relative resistance with increasing relative length of the strained sample during loading and unloading. The short dotted and the solid curve show the difference between measured (R_{meas}/R_{0meas}) and the corrected (R_{samp}/R_{0samp}) relative resistances. The dashed line, labelled as Eq. (4) corresponds to the constant volume assumption of Equation 8. Eq. (3) can be neglected [16].*

2.4 Deformation behaviour of metal films on compliant substrates

2.4.1 Shear lag theory for brittle metal films

The deformation behaviour of brittle films on compliant substrates has been examined in more detail over the last decade [4-6, 24]. It has been observed that there is no longer a direct force transmission to the film as soon as fracture starts due to the formation of cracks. All further loading must then be transferred to the film across the interface. However, the interface can only sustain a limited level of shear stress. Once this interfacial stress has been reached either the interface or the neighbouring substrate is expected to yield. With increasing strain, the yielded area will spread along the interface until a saturation stage of cracks is reached (also called steady state). At this point, the interface has yielded along its complete length and therefore, no further cracks can be formed although straining continues. The interfacial shear stress depends on the film thickness, the fracture stress of the film and on the crack spacing in the steady state, as given by Equation 2 in Section 2.2 [9,10].

The brittle failure behaviour is schematically plotted in Fig. 2.4, showing both fracture stress and shear stress as function of the distance between two cracks. At the positions $x = 0$ and $x = L$, where first cracks have arisen, the film cross section is stress free. The earliest

point between zero and L for forming a new crack is the position at which the fracture strength is first reached. This distance is called the minimum fracture length, λ_{min}, see Fig. 2a. Indicated in Fig. 2.4b, no further fracture of the film can occur, if the distance between the cracks is not larger than two times λ_{min}. This is because the transfer of the shear stress over the interface is just sufficient to reach the fracture stress of the film in the centre of this segment. Thus, any segment longer than this maximum fracture length, $\lambda_{max} = 2\lambda_{min}$, would be expected to fracture until all segments lie between λ_{min} and λ_{max}. Then no further fracture can occur and the saturation stage is reached.

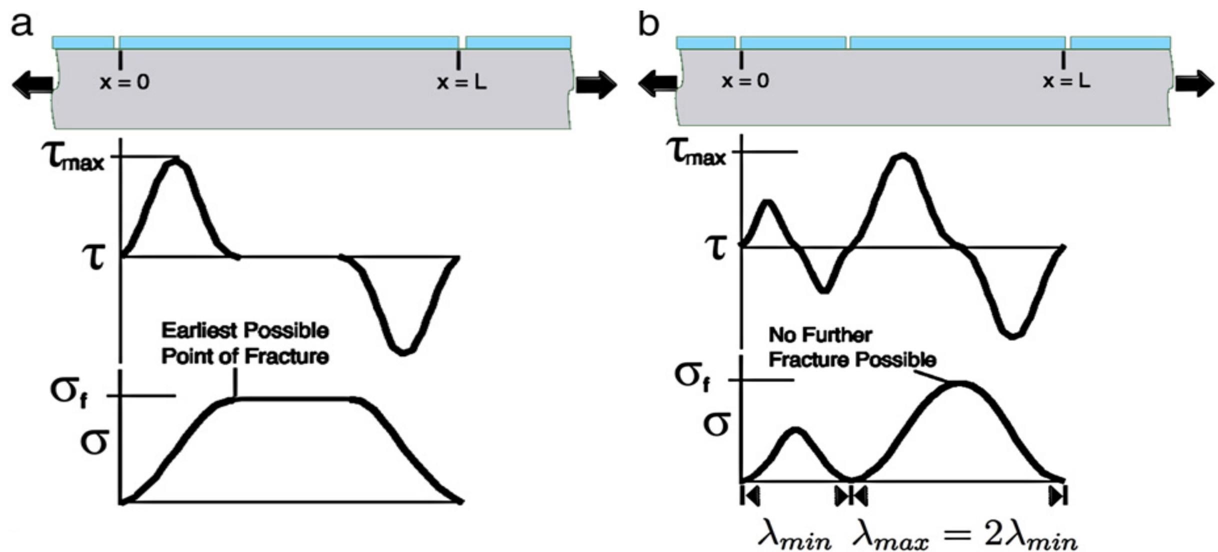

Fig. 2.4. *Schematic diagram of the brittle failure behaviour of thin metal films showing both failure stress and shear stress as function of the distance between two cracks. (b) If $\lambda_{max} = 2\lambda_{min}$ no further fracture of the film happens [9].*

It should be noted that this behaviour only occurs if the fracture strength is single-valued. In reality, however, this is not the case and the fracture strength of brittle films is better described by a Weibull distribution. Moreover, film thickness inhomogeneities can alter the measured interfacial shear strength data seriously. Taylor et al. have especially shed light on how roughness and waviness of the film influence the crack spacing [9,10].

2.4.2 Ductile metal films

Experiments have shown that there is an essential difference in the deformation behaviour between a freestanding and a substrate bonded ductile metal film. Freestanding films usually rupture at small strains [25,26], whereas thin metal films on compliant substrates (e.g. polymer) show a broad distribution concerning their failure strains ranging from less than one

percent to a few tens of percent [19, 27-30]. Exposed to a tensile strain, a freestanding thin metal film deforms uniformly. When the tensile strain is large enough to break the oxide layer surrounding the freestanding film, dislocations can easily escape at the film surface at a local spot and no further hardening of the film happens there. Thus, this perturbation in the film thickness promotes the film to thin locally and to form a neck. Further deformation is localized in the formed neck, which leads to the film's rupture, as shown in Fig. 2.5a. At the site of rupture, strain localization causes a large local elongation on the order of the film thickness [31-34].

On the other hand, for brittle films rupture starts by breaking a single array of atomic bonds without local elongation of the film. Consequently the presence of a polymer substrate does little to prevent the film from cleaving (Fig. 2.5b), but it does reduce the driving force on a formed channel crack by limiting the opening in its wake [33].

For ductile metal films bonded to a substrate, the geometric constrain caused by the substrate decelerates strain localization (Fig. 2.5c). Hence, the metal film deforms uniformly to a large strain. However, if the metal film debonds from the substrate (i.e. the film becomes freestanding), the substrate cannot suppress necking, which subsequently leads to the film's failure. This is shown schematically in Fig. 2.5d [31-34]. Therefore, it is believed that good adhesion is required for desirably high failure strains. The interfacial adhesion can be increased with prior surface treatments to the substrate or by adding thin adhesion layers between substrate and metal film. Nevertheless, it should be anticipated at this point, that increasing adhesion by adding layers may not work well when heat treatments are used. Due to the heat, diffusion and new phases could form, which weaken the interface and lead to premature fracture [35].

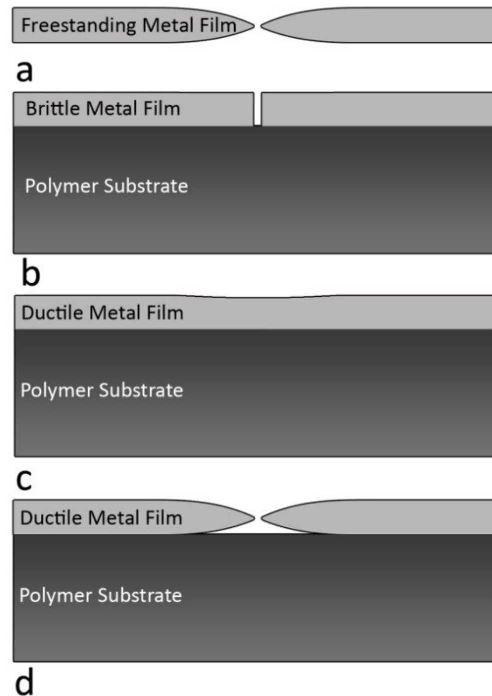

Fig. 2.5. *Schematic of the deformation behaviour of (a) a freestanding ductile thin metal film, (b) a brittle, substrate bonded metal film (c) a ductile thin metal film well bonded to a substrate and (d) a ductile thin metal film debonding from the substrate.*

2.4.3 Effects on the deformation behaviour of thin film systems

Besides strong adhesion, uniform deformation behaviour of the metallic film is important in order to achieve large failure strains. This depends strongly on the present microstructure of the film. Without thermal treatment, the microstructure of as-deposited Cu films can be unstable under mechanical loads. As-deposited sputtered films mostly consist of nano-sized grains with a few submicron grains randomly distributed in the matrix. Due to the Hall-Petch effect, these nanocrystalline sections have a high yield strength and are more difficult to plastically deform than the larger grains. Thus, the deformation initiates in the larger grains, which behave like soft inclusions embedded in a hard matrix. With increasing strain, nanocrystalline grains in regions of strain localization (i.e. near large grains) start to grow and weaken the material locally. Tractions originate on the film-substrate interface with ongoing localization, causing local delamination of the film. The film locally loses the constraint of the underlying substrate and necks and isolated micro-cracks can form. At higher strains the cracks become interconnected. The described failure mode of as-deposited Cu films is drafted in Fig. 2.6 [14].

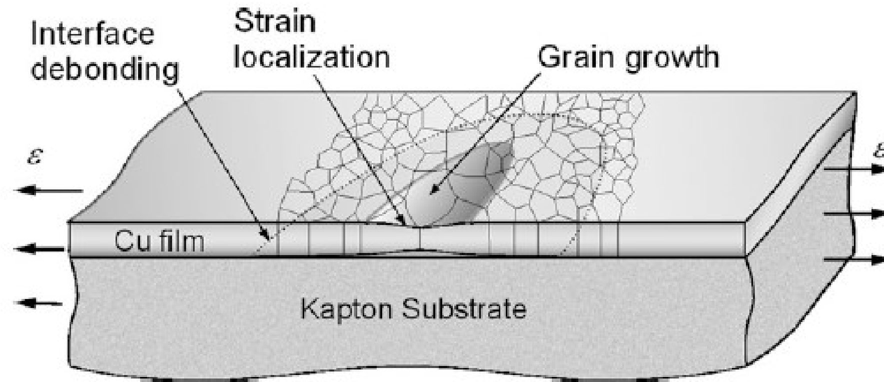

Fig. 2.6. *Schematic diagram of the microstructural changes in a Cu film on Kapton during straining. For forming a neck, three things coevolve: deformation-associated grain growth, strain localization promoted by large grains and the local delamination of the film from the substrate [14].*

The deformation behaviour of annealed Cu-films on polymer substrates is distinctly different. Annealed samples have a more uniform microstructure with grains in the micrometre range. Hence, their microstructure remains stable under deformation and no grain growth takes place. The sample deforms relatively homogeneous until simultaneous delamination and strain localization lead to the sample's fracture. The difference in the deformation behaviour between as-deposited and annealed films is also illustrated in Fig. 2.7 and Fig. 2.8. Fig. 2.7 plots the normalized resistance, R/R_0, as a function of the normalized length, L/L_0, showing the deviation from a fully homogenous deformation without crack formation and growth. The theoretical prediction (dashed line) assumes the ideal case of missing crack formation during straining. Thus, as long as the curves follow the trend, the films' volumes remain constant. With further increase in strain, damage will be induced in the film and the existence of micro-cracks will increase the electrical resistance substantially. The as-deposited curve deviates earlier and stronger from the theoretically predicted line as the annealed one, so the formation and propagation of cracks start at an earlier stage leading to a higher crack density and to the interconnection of micro-cracks [14,36].

Due to the heterogeneous microstructure of the as-deposited films, their stress-strain curves exhibit a gradual transition from the elastic to the plastic regime, as shown in Fig. 2.8. As already mentioned above, different sized grains yield at different stress levels creating a rounded stress-strain curve. For thicker films the transition is even more gradual, because of their wider grain size distribution. In contrast, annealed films have a sharp elastic-plastic transition. Thanks to diffusional processes, the stress in the film is almost relaxed after annealing. After cooling to room temperature a tensile stress develops in all grains due to the

thermal mismatch between film and substrate. Hence, all grains yield at more or less the same strain with minor variations owing to the anisotropy of the grains [37].

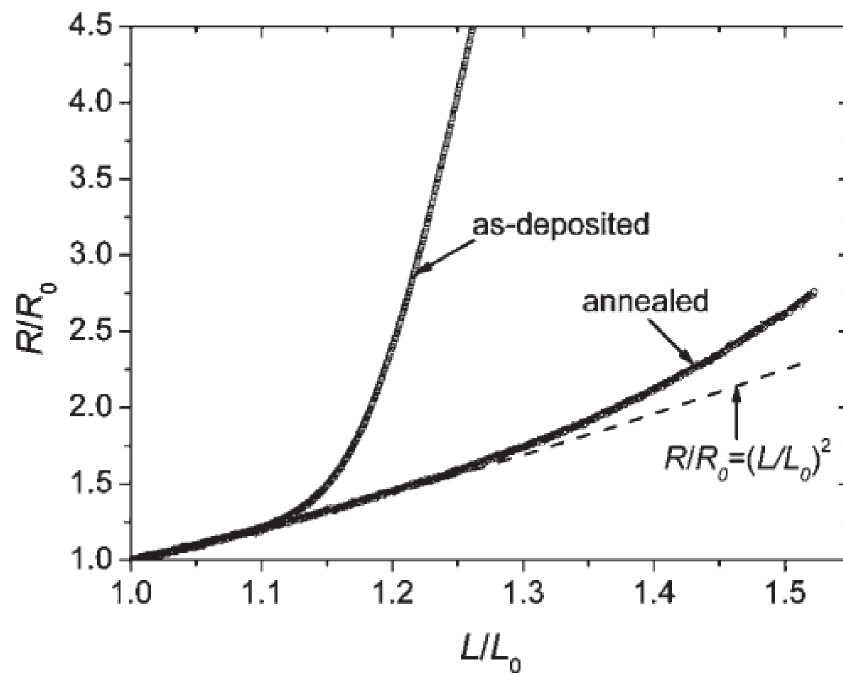

Fig. 2.7. *Relative resistance, R/R_0, as a function of the relative length, L/L_0, for as-deposited and annealed Cu films compared to the constant volume assumption ($R/R_0 = (L/L_0)^2$) [14].*

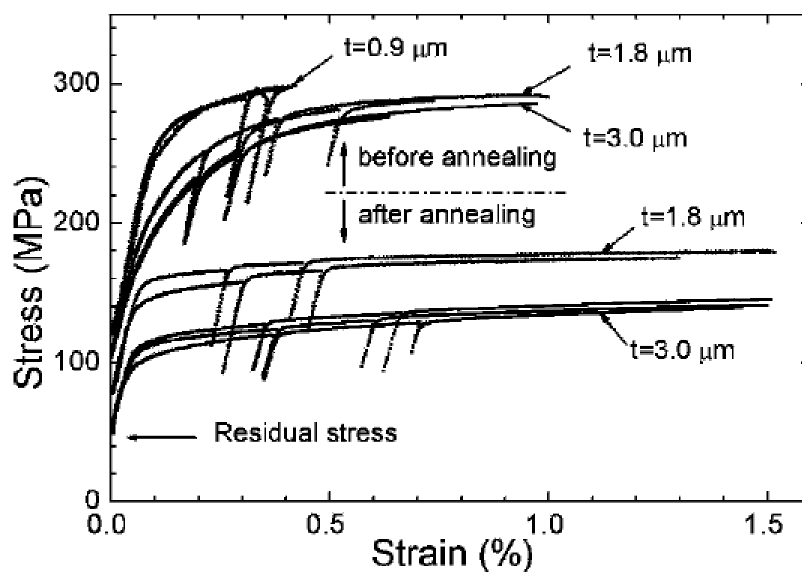

Fig. 2.8. *Stress–strain curves of freestanding Cu films with variations in thickness before and after annealing. Differences in yield stress and transition from the elastic to the plastic deformation behaviour can be explained with the respective microstructure [37].*

The film thickness also influences the deformation behaviour of copper films, as illustrated in the resistance plot in Fig. 2.9. Generally, the thinner the film, the smaller the failure strain and as a result the curve starts to deviate from the theoretical line ($R/R_0 = (L/L_0)^2$) earlier. Thus, with decreasing film thickness, the crack density distinctly increases. Films with thicknesses greater or equal to 500 nm can withstand large strains without forming TTCs. These films rupture due to simultaneous debonding and necking. The 200 nm films show more trans-granular cracking than the former mentioned. The failure mode changes from ductile to brittle for films with thicknesses equal to or smaller than 100 nm. Instead of transgranular crack paths, the forming crack spreads along the grain boundaries. These intergranular cracks are often interconnected and form long transverse cracks, which influence the film's conductivity unfavourably. The films fail at relatively small elongations due to grain boundary decohesion. Having a more precise look at Fig. 2.9, it is striking that the 1 µm film deviates earlier from theory than the 500 nm film. The reduced strain-to-failure of the 1 µm film is directly linked with its crystallographic structure. In contrast to thin films of face-centred cubic metals (e.g. Cu), which tend to have a strong (111) texture, thicker films also exhibit a (100) texture component. This component increases with film thickness. Due to the fact that grains with a (100) orientation have a much lower flow stress than (111) orientated grains, the (100) orientated "inclusions" deform more easily, which leads to strain localization and results in transgranular fracture. As a consequence of the larger fraction of (100) grains in the 1 µm film, the failure strain decreases with film thickness above 500 nm, as shown in Fig. 2.10 [15].

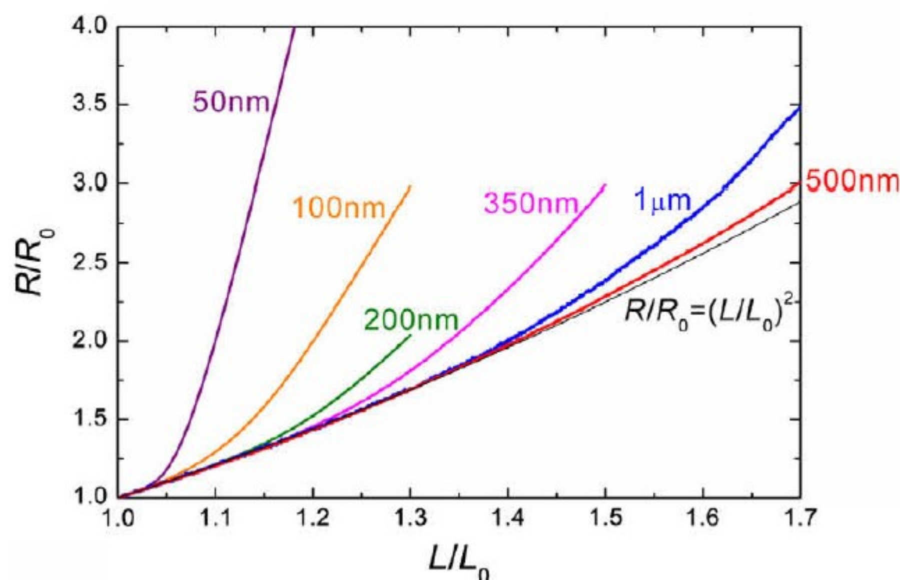

Fig. 2.9. *Relative resistance, R/R_0, as a function of uniaxial film elongation for sputtered Cu foils on PI with variation in their film thicknesses. $R/R_0 = (L/L_0)^2$ describes the constant volume assumption [15].*

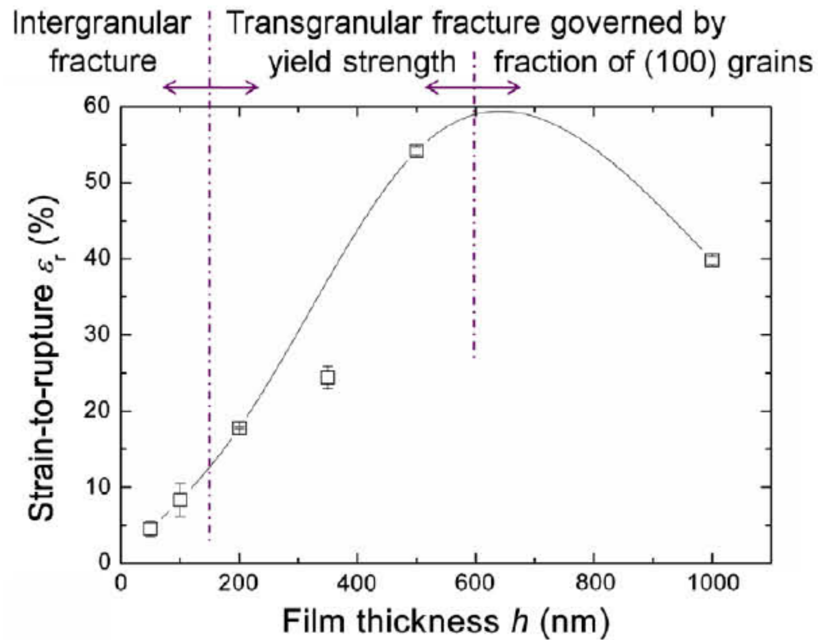

Fig. 2.10. *Change of the failure strain, ε_r, with increasing film thickness, h, due to different fracture behaviours [15].*

3 Experimental

3.1 Film deposition

Four different thin film systems were produced for testing: 50 nm, 100 nm and 200 nm Cu films on PI, whereupon some of the 200 nm thick films were further heat treated at 200 °C for 1 hour without breaking vacuum. All films were deposited using electron beam evaporation onto cleaned 50 µm UPILEX brand PI. The vacuum in the deposition chamber varied slightly between start and ending of the deposition process ($5*10^{-7}$mbar - $2*10^{-7}$mbar). For the 100 nm and 200 nm Cu films, a deposition rate of 5 Å/s was chosen, for the 50 nm thick foils, however, the deposition rate was only 3 Å/s. Samples sized 6 x 35 mm were cut out of the different Cu-PI-sheets.

3.2 Microstructure determination

The microstructure of the Cu films was determined using electron backscatter diffraction, focused ion beam and transmission electron microscopy depending on the film thickness. For this thesis, contrast and brightness of SEM, TEM and FIB micrographs were adjusted to improve the distinguishability.

3.2.1 200 nm thick Cu films on PI

The grain size of the 200 nm thick Cu films, both as-deposited and annealed, was characterized in a scanning electron microscope type LEO 1525 using TSL OIM Data Collection version 5.31 for making EBSD scans. Typical settings were an accelerating voltage of 20 kV, a working distance between 0.5 cm and 1 cm and a 70° tilt of the examined sample. In average, three EBSD scans were made, with magnifications between 5 and 10 kX. The step size for scanning was between 0.05 and 0.1 µm, depending on the image size. For scans with larger dimensions, a larger step size was chosen to limit drift during scanning. Furthermore, for preventing drift, a Cu tape was directly positioned next to the area of interest before inserting the film in the vacuum chamber of the SEM.

The grain size determination was made with the help of the EBSD software TSL OIM Analysis version 5.31, fixing the following parameters for all scans. The confidence index was set to be 0.05 and all grains not meeting this criterion were coloured black in the scan. Moreover, a grain had to exhibit at least five pixels with the same orientation in order to be defined as a grain. Two ambient grains had to lie under a minimal angle of 15° to each other in order to be counted as a grain. Grains, which were cut off at the edge of the screen, did not

contribute to the analysis. As a final setting, recrystallization twins were not evaluated as extra grains. Besides number and diameter of grains, the misorientation angle and the crystallographic orientation of the grains were also calculated by the software.

In addition to the EBSD scans, ion channelling contrast images were taken with the FIB to present the microstructure in better resolution.

3.2.2 Cu films with film thicknesses below 200 nm

The microstructure of the 50 nm and the 100 nm thick Cu foils was characterized by plan view TEM micrographs. For imaging in the TEM, the Cu foil was scraped off the substrate with a razor blade and then positioned on a 10 – 15 nm carbon coated 200 mesh copper grid (brand "Plano" [38]) [39]. The surface area of 30 – 40 grains was measured using ImageJ [40]. Clearly identified grains were traced and the area inside the shape was calculated. Therefore, the diameter of the grain could be determined.

3.3 In-situ fragmentation testing under the AFM

In-situ AFM fragmentation testing is applied to characterize the surface deformation of Cu films on PI depending on film thickness and microstructure. Furthermore, with the aid of this method, localized thinning of the film in the form of necks and through thickness cracks can be distinguished.

3.3.1 Test execution

For performing the in-situ tensile tests, a custom built, miniaturized straining device was used. The displacement was controlled manually using a screw-driven mechanism. The load on the sample could not be measured with this device. The elongation of the strained sample was determined using an external measurement system, more precisely by use of a high precision calliper. The minimum initial gauge length was about 18 mm in order to accommodate the AFM head and the tip; the maximum displacement of the grips was approximately 25 mm. For imaging the films' surfaces, which were held under tension during the whole experiment, a DI Dimension 3100 AFM was used in tapping mode. Moreover the highest available image resolution of 512 dpi and a scanning rate less than 1 Hz were chosen for imaging, in order to get relatively high quality images. With these settings, each image took about 10 – 20 minutes for a scan size of 25 µm x 25 µm. The used AFM tips were Nanosensors™-PointProbe® Plus – NCHR with a guaranteed radius < 10nm.

For the in-situ tensile test, a specimen of the size 6 mm x 35 mm was mounted between the two grips of the loading device. To see the change of the sample's surface with

increasing strain, the Cu film was marked in order to find the same spot for all images. When the sample was firmly fixed in the grips by consecutively tightening the screws, the distance between the grips was increased to remove any slack of the sample. Consequently the sample should be tight, but not yet strained. This distance between the grips was measured and recorded as the initial gauge length. The device was then positioned under the AFM and the tip was lowered. As a next step, a region close to the marking was chosen, ideally with a recognizable surface feature. The surface inhomogeneity should not be too large, because this might lead to loss of contact of the AFM tip to the sample's surface while scanning. For one sample, all images were taken at the same area with two different scan sizes (25 µm x 25 µm and 10 µm x 10 µm) after increasing the strain, ε, form $\varepsilon = 0\%$ in steps. Moreover, for each straining step both an amplitude and a height image are recorded perpendicular to the straining direction. After disassociating the tip from the surface, the displacement was increased, the new gauge length was measured and the tip was lowered again. Then the same region of the film had to be found once more making use of the surface marking. Subsequently, the film was imaged again in the same area, repeating the process for every straining step until the desired maximum strain was reached or the sample broke. The engineering strain, ε, was calculated for each individual straining step as the ratio between the current length variation, ΔL, and the initial gauge length, L_0 (Equation 12).

$$\varepsilon = \frac{\Delta L}{L_0} \tag{12}$$

3.3.2 Analysis

Every suitable height image was analysed with Gwyddion [40], a free software for visualizing and analysing data from scanning probe microscopy techniques like the AFM. Each image was plane levelled and scanning defects due to the AFM were removed by line corrections. Moreover the minimum height value of the scanned AFM image was set as zero point of the height scale. Therefore, note the different height scales used in the AFM images for comparing the data. Three vertical surface profiles (cross sections) with approximately the same distance to each other were taken across an entire image. These profiles were positioned at nearly the same area for each straining step. With the aid of these profiles the deformation and the through thickness crack density could be determined by counting the number of necks and TTCs and just TTCs intersecting the line (see Equation 2), respectively.

As an example of deformation spacing measurement, AFM height images at different strains with the corresponding surface profiles are shown in Fig. 3.1 and Fig. 3.2 for a 50 nm

Cu film on PI. The AFM height images show approximately the same area for all three images. For the data analysis, all of the images have been evaluated, not only the three shown here. Furthermore, for the analysis three surface profiles on each image have been made instead of one, as it is shown. The figure shows only one surface profile in order to explain the method more clearly. Through thickness cracks are marked with black arrows in both the AFM images and the height profile, whereas for better clarity necks are just indicated in the latter with grey arrows.

The deformation spacing, $\lambda_{def.}$, corresponds to the average distance between two deformation sites (necks and cracks), while the crack density only takes into account the TTCs, as shown in Fig. 3.3. To distinguish between necks and cracks, the ratio between the average deformation depth, Δ, and the film thickness, h, has to be determined. Therefore, the position of each minimum of the height profile in the AFM image was recorded. To determine Δ, the average difference between the value at the minimum and five values to the left and right was calculated. The averaged depth value normalized to the film thickness, Δ/h, tells which percentage of the film thickness the deformation occupies. With the aid of Equation 4 and Equation 5, cracks and necks could now be distinguished. As an addition to these criteria, Δ/h ratios under 2% were defined as surface roughness and were therefore ignored in the analysis.

For comparing the deformation behaviour observed under the AFM for the different film thicknesses, $\lambda_{def.}$ is plotted as a function of strain as shown in Fig. 3.4. In addition to the deformation spacing, the crack spacing, λ_{crack}, defined as the average distance between two cracks, is also depicted for the 50 nm thick Cu film.

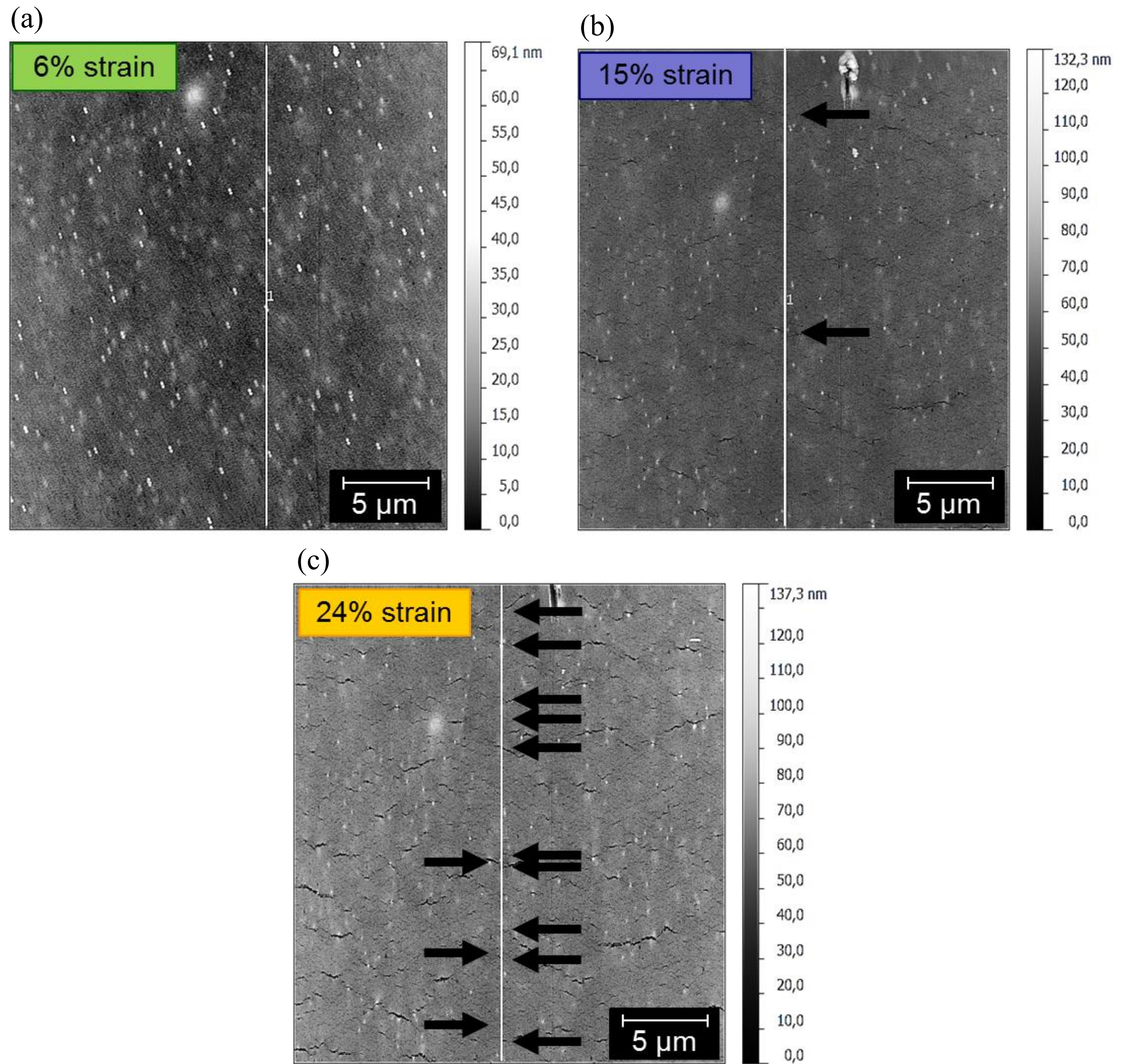

Fig. 3.1. *AFM images with surface profiles at (a) 6% strain, (b) 15% stain and (c) 24% strain of a 50 nm Cu film. Positions of channel cracks are indicated with black arrows. Note the different height scales used in the AFM images.*

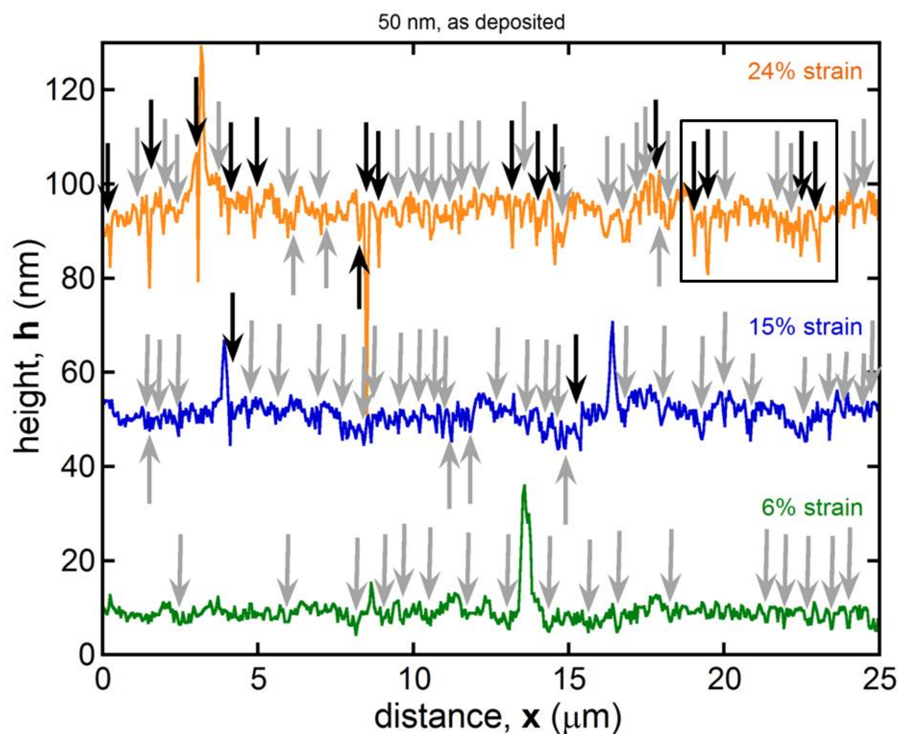

Fig. 3.2. *Surface profiles of the 50 nm Cu on PI from Fig. 3.1(a), (b) and (c) indicating where necks and TTCs have formed. Gray arrows represent necks and black arrows TTCs.*

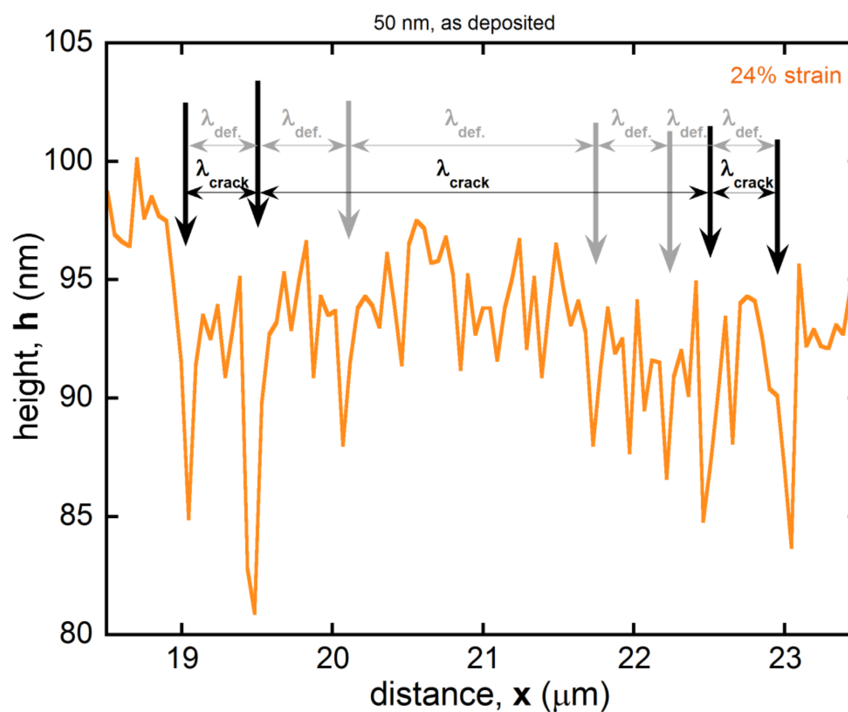

Fig. 3.3. *Segment of Fig. 3.2 expressing the difference between deformation spacing,* λ_{def}*, and crack spacing,* λ_{crack}*. The deformation spacing corresponds to the average distance between two deformation sites (necks and cracks), whereas the crack spacing just defines the average distance between two cracks.*

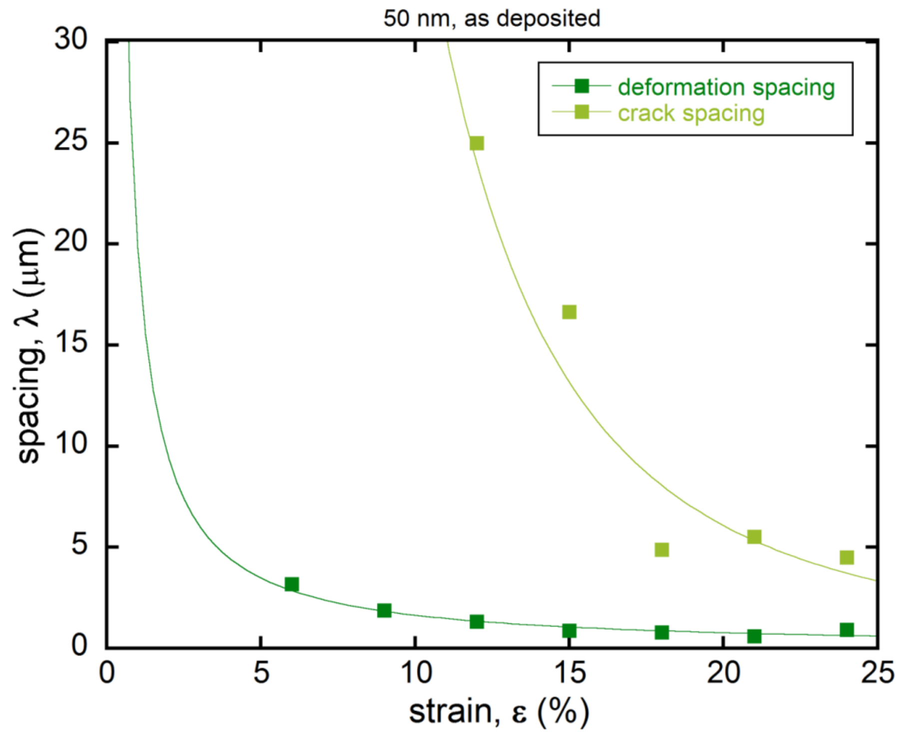

Fig. 3.4. *Evolution of crack and deformation density as a function of strain for the in Fig. 3.1 shown AFM experiment of a 50 nm Cu film. Necks arise at about 6% strain and cracks start forming at approximately 12% strain. The fitted line through the data points is just to guide the eye.*

3.4 In-situ resistance measurements

Tensile tests with in-situ resistance measurements were performed on an MTS Tyron 250® Universal testing machine with a constant displacement rate of 5 µm/s for loading and unloading. For each film system, four tests were executed, each with a maximum strain of 20%. The initial gauge length, L_0, for all specimens (6 x 35 mm) was approximately 20 mm and the sample's elongation, the load on the sample and the time were measured automatically by the straining device. The 4PP in-situ resistance measurements were taken with a Keithley 2000 multimeter with the probing contacts incorporated into the grips. The schematic of the 4PP resistance measurement setup, inclusive an image of a mounted sample, is shown in Fig. 3.5. All experiments were performed at room temperature and in air.

Before starting the experiment, the sample's width was measured with a high-precision calliper. Furthermore, the initial resistance of the sample, $R_{0sample}$, was determined by a second 4-point-probe resistance measurement setup, shown in Fig. 3.6. Here the distance between the inner contact needles was only half the gauge length of the straining device and

therefore the measured resistance had to be doubled in order to compare it to that measured during straining.

After mounting the sample between the grips of the straining device, the specimen was strained just as much as to remove any slack in the sample. The gap between the grips equaled the initial gauge length. Before actual straining the initial resistance, R_0, had to be recorded for approximately 15 minutes in order to be sure that it remained constant. The constant value was then recorded as R_{0meas}. Simultaneously with the straining, the resistance measurement had to be started. The measured resistance, R_{meas}, was recorded by the ohmmeter as a function of time. By multiplying the time with the displacement rate and normalizing it to the measured initial gauge length, the resistance could be expressed as a function of the elongation. Furthermore, in order to determine the real resistance of the sample, R_{samp}, R_{meas} had to be corrected by subtracting the resistance of the film under the grips, R_{const}, according to Equation 9.

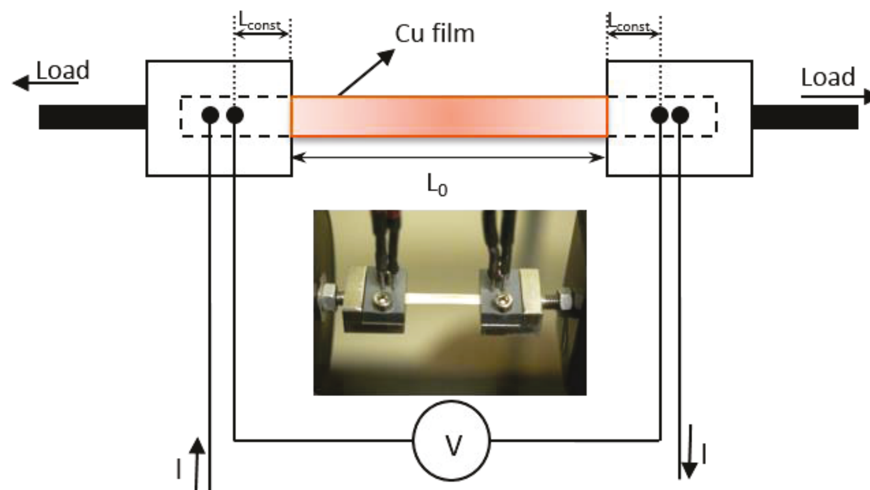

Fig. 3.5. *Schematic diagram of the used 4PP resistance measurement setup. For clear understanding, the probing contacts were plotted further apart. Meanwhile, they are positioned at the inner edge of the grips. Thus, L_{const} can be assumed as zero and the distance between the probing contacts equals the gauge length. The initial gauge length, L_0, is 20 mm. The inset photo shows a mounted sample between the grips of the straining device [16].*

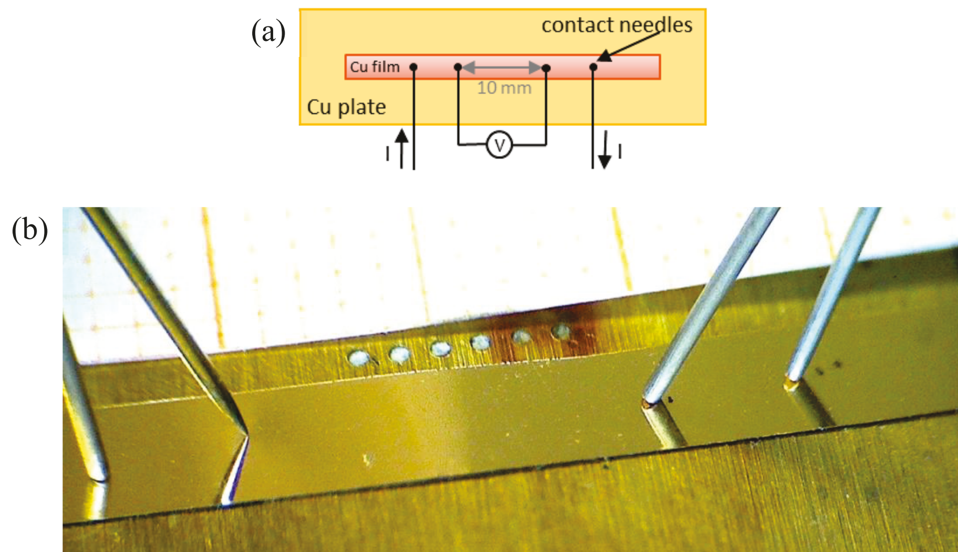

Fig. 3.6. (a) Schematic and (b) photo of the 4PP resistance measurement setup for determining R_{0samp}.

3.5 In-situ EBSD tensile tests

To observe if a change of the microstructure occurred with increasing strain, in-situ tensile tests in the SEM were additionally performed for the as-deposited and the annealed 200 nm thick Cu foils. For realizing these tests, the examined films were mounted between the grips of the custom build, screw driven straining device used for the AFM experiments. The device was then fixed on the SEM stage in order to be able to tilt the whole system 70°. For accommodating the tensile device, the working distance had to be enlarged to 17 – 20 mm. All the other settings were chosen as documented in section 3.2. To increase the strain, the vacuum chamber was vented and opened and the sample was further strained using a hex tip screwdriver.

3.6 Post-mortem determination

After the tensile tests, the already strained films were examined under the AFM and with the SEM to check if a time dependent relaxation state of the Cu-PI-compound existed and to characterize the deformation and possible cracking.

4 Microstructure characterization

The resulting grain size distributions determined with TEM and EBSD micrographs are shown in Fig. 4.1 and Fig. 4.2. The 50 nm and 100 nm thick Cu films were strained up to 20%, and the 200 nm films for 21% before imaging. Strained samples were taken for the analysis because of the used TEM sample preparation technique [39]. The used scrape technique requires that the films are strained prior to removal, so that more film fragments are present on the TEM grid. It is not believed that the straining increases the grain size since the measured grain size is below the film thickness. It is obvious from Fig. 4.1 that the 50 nm and the 100 nm films mainly consist of nano-sized grains with average grain size values a little bit below the film thickness. The averaged grain size of the as-deposited 200 nm films is in the range of the film thicknesses. However, these films also exhibit randomly distributed µm-sized grains making the grain size bimodal. With annealing, the percentage of µm-large grains increases. The average grain sizes of all investigated Cu films on PI are listed in Tab. 4.1 with their standard deviations. Moreover, FIB and TEM plan view images of the four different samples are shown in Fig. 4.3 and Fig. 4.4.

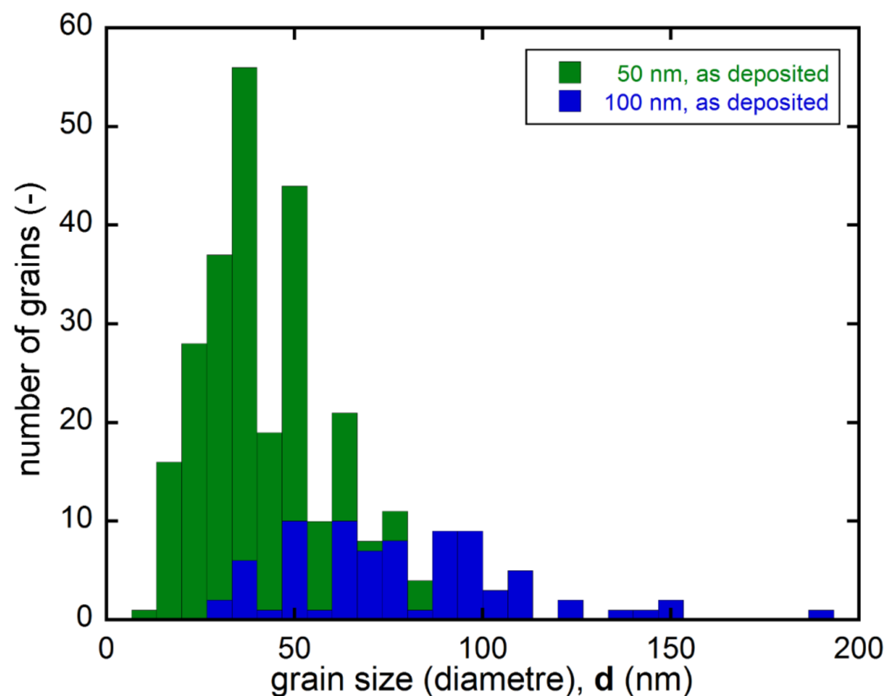

***Fig. 4.1**. Grain size histograms of 20% strained, as-deposited 50 nm and 100 nm thick Cu films. Grain sizes were characterized at plan view TEM micrographs.*

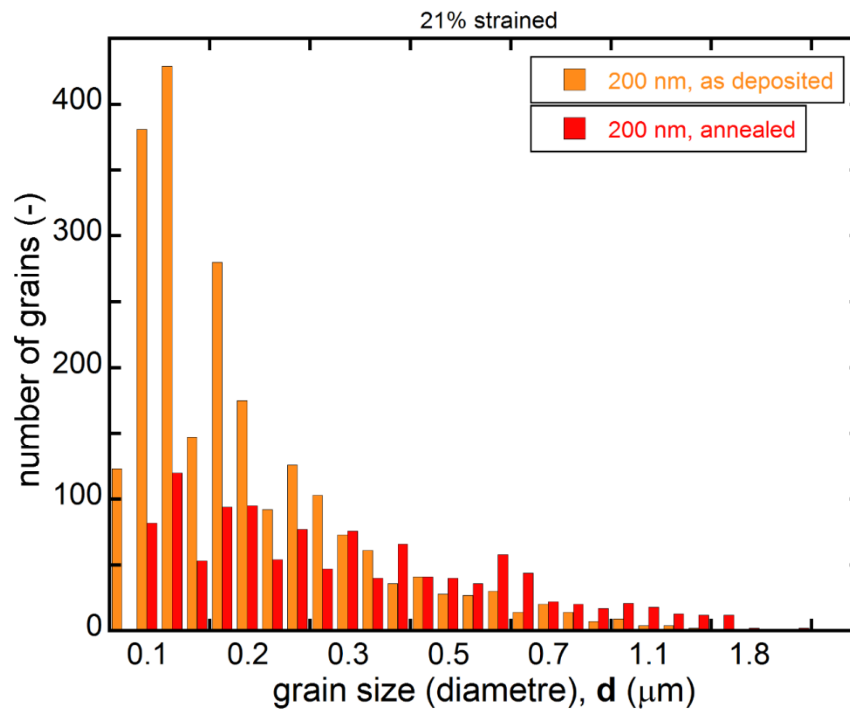

Fig. 4.2. *Column diagrams showing the different trend in grain size distribution between as-deposited and annealed 200 nm Cu films, both strained to 21%. Grain sizes were determined by the EBSD software TSL OIM Analysis version 5.31.*

Tab. 4.1. *Average (av.) grain size and its standard deviation listed for as-deposited and annealed Cu films on polyimide. The standard deviations for the 200 nm thick films are huge due to their bimodal grain size.*

Cu films on PI	film thickness, h (nm)	av. grain size, d (nm)
as-deposited	50	38.5 ± 14.3
as-deposited	100	77.2 ± 30.2
as-deposited	200	209.1 ± 153.2
annealed	200	379.6 ± 323.7

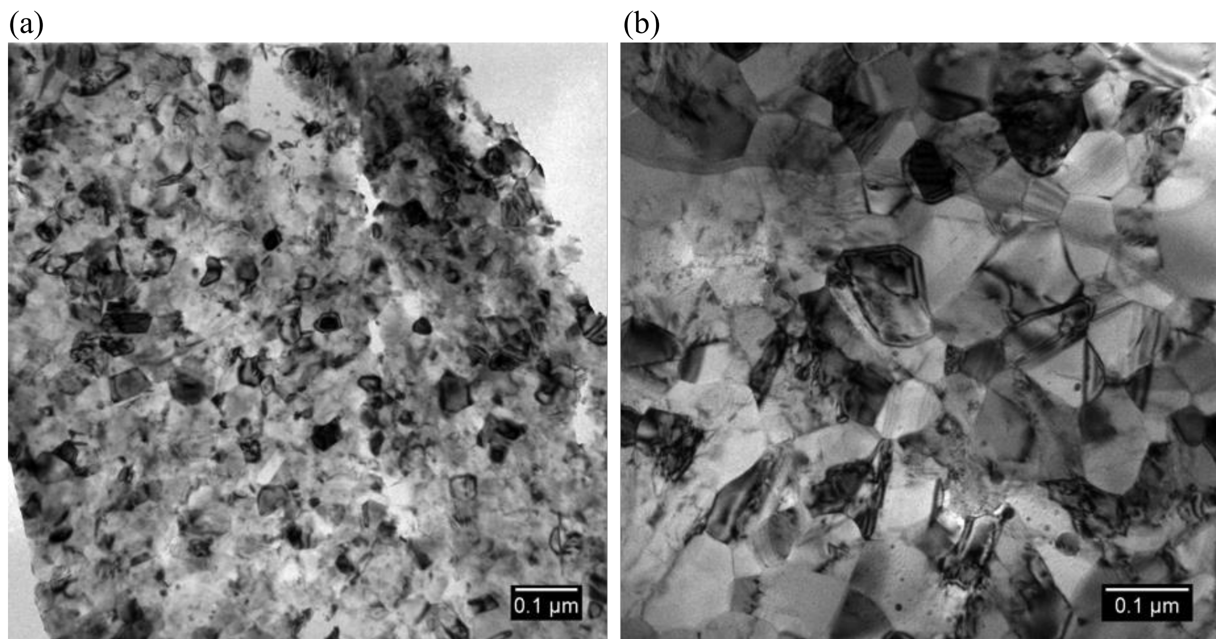

Fig. 4.3. Plan view TEM micrographs of (a) a 50 nm and (b) a 100 nm thick Cu film. Images taken by V. Maier.

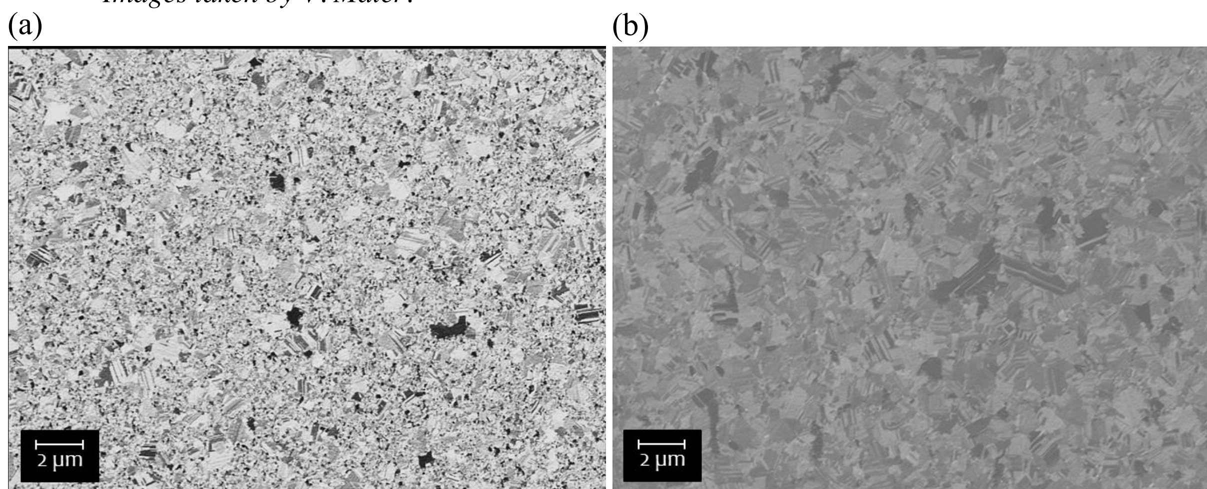

Fig. 4.4. Ion channelling contrast images of (a) the as-deposited and (b) the annealed 200 nm thick Cu film, illustrating the bimodal grain size of the as-deposited compared to the more homogeneous grains of the annealed film. Taken by (a) B. Völker and (b) R. Treml.

The microstructure of the 200 nm films was examined in more detail with the aid of EBSD orientation maps, as shown in Fig. 4.5a and Fig. 4.5b. Grains coloured blue, red and green possess a (111), (100) or (101) orientation, respectively. It is obvious from Fig. 4.5 that there is no preferred orientation, neither in the annealed nor in the as-deposited film. The grain alignment is relatively random with just a few more (111) and (100) orientated grains, as depicted in the pole figures (Fig. 4.5d and Fig. 4.5e).

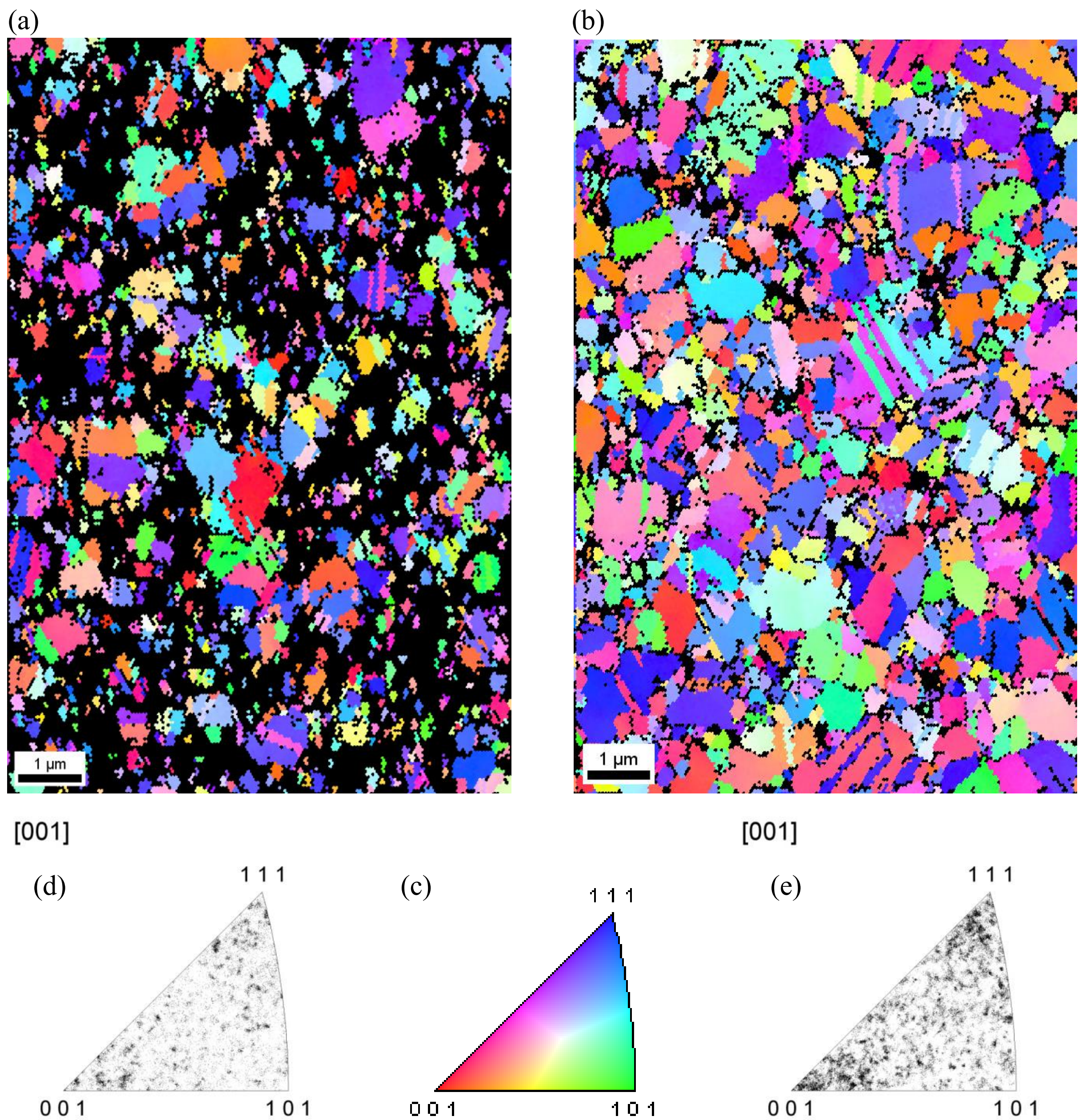

Fig. 4.5. *EBSD orientation maps of 200 nm thick Cu films (a) without and (b) with heat treatment (200° C, 1 h) strained to 21%. The orientation of the grains is represented with the help of the orientation colour key (c). The confidence index was set to be 0.05; all grains not meeting this criterion are coloured black in the scan. Relatively random grain alignment with slightly more (111) and (100) orientated grains for both films, the as-deposited (d) and the annealed film (e).*

In addition to the EBSD scans of the already strained Cu films, in-situ tensile tests were performed in the SEM in order to determine if grain growth occurred during straining. In the beginning it was attempted to scan the same area for all straining steps, but the surface was locally destroyed due to the sample's charging. So scanning the same spot could not deliver reliable results, as shown exemplarily in Fig. 4.6 for an annealed film. The first EBSD scan was made at 0% strain (Fig 4.6a). A second image was taken after increasing the strain to 5%, showing exactly the same surface area (Fig. 4.6b). Scanning this area for a third time at 10% strain, however, led to more than 50% undefined surface (coloured black in Fig. 4.6c). Moreover, the identified grains are elongated, which is an indication for drift and surface charging.

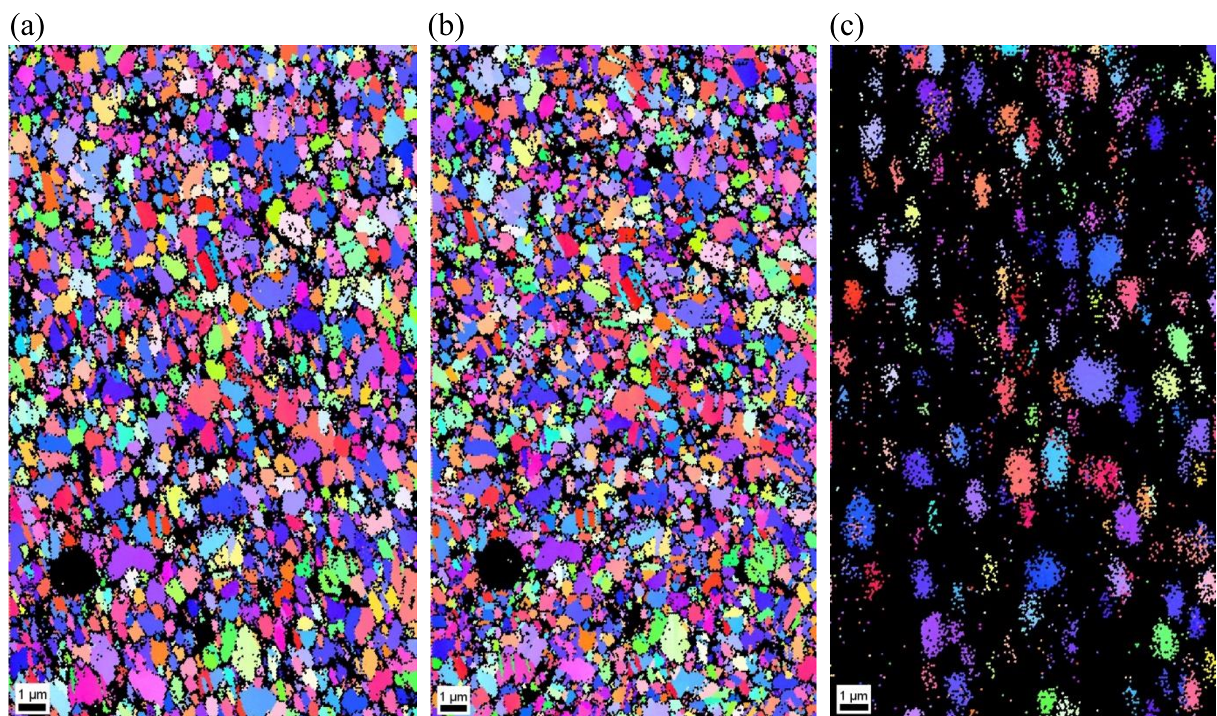

Fig. 4.6. *EBSD orientation maps of an annealed 200 nm Cu film showing the same spot for (a) 0% strain, (b) 5% strain and (c) 10% strain.*

Thus, different areas in close proximity to each other were used for scanning for the in-situ experiment in the SEM. For each straining step, the average grain size of all imaged areas was determined. The grain size did not change with increasing strain for the as-deposited nor for the annealed Cu film, as summarized in Tab. 4.2. Grain growth during straining is not a present mechanism in Cu films deposited via electron beam evaporation, which is contrary for as-deposited sputtered Cu films as shown by Lu, et al. [4]. Straining as-deposited, evaporated,

200 nm thick Cu films with a bimodal grain size under cyclic loading conditions, however, leads to the in [4] observed grain growth, as executed by O. Glushko [13].

Tab. 4.2. *Average (av.) grain size inclusive standard deviation for different straining steps of an as-deposited and an annealed 200 nm thick Cu film determined out of the in-situ EBSD data. The standard deviations are huge due to the bimodal grain size showing large-μm grains in a nano-sized matrix.*

as-deposited 200 nm thick Cu foil		**annealed 200 nm thick Cu foil**	
strain (%)	**av. grain size (nm)**	**strain (%)**	**av. grain size (nm)**
0	309.8 ± 200.5	0	449.7 ± 314.1
6	340.9 ± 176.5	5	420.6 ± 303.3
		10	418.5 ± 299.9
13	294.3 ± 173.3	15	358.7 ± 248.3
21	264.5 ± 293.5	20	407.2 ± 252.2

5 Fragmentation testing under the AFM

5.1 Effect of film thickness

As an example of deformation spacing measurement, AFM height images at different strains with the corresponding surface profiles were shown for a 50 nm Cu film on PI in Fig. 3.1 and Fig. 3.2. At the observed surface position, only necks (grey arrows) are present after a strain of 6%. Cracks (black arrows) have not formed yet. With increasing strain two things happen. First of all, the number of necks rises and secondly, some of these previously formed necks increase in depth and become cracks. Comparing the height profile at 15% strain with the one at 24% strain, it is observable that the sum of necks and cracks is pretty much the same for both. So at about 15% strain, the deformation spacing remains roughly constant. This behaviour can even better be seen in Fig. 3.4, where both deformation spacing and crack spacing are plotted against the strain. The lines fitted through the individual data points do not have any mathematical meaning and they just should help to guide the eye. First signs of necks can be detected with the AFM at 6% strain with an average spacing of 3 µm. Deforamtion spacing decreases with increasing strain and levels out at about 15% strain. The average saturated deformation spacing, $\lambda_{\mathrm{sat.(def.)}}$, is ~ 0.8 µm. First cracks appear after an elongation of ~ 12% average 25 µm apart from each other. With increasing strain, crack spacing falls until it saturates at 18% strain with $\lambda_{\mathrm{sat.(crack)}}$~ 5 µm.

The major difference in the deformation behaviour between a 50 nm and a 200 nm thick Cu film is the absence of cracks in the latter one. Although all films have been strained to 24% under the AFM, only the 50 nm specimen showed frequent cracking. In Fig. 5.1, the AFM height images inclusive surface profiles for all three film thicknesses are shown at saturation stage. In the tested 100 nm sample, a single crack was detected at 18% strain, as depicted in Fig. 5.1b. Comparing the surface profiles plotted in Fig. 5.1, a transition from brittle to ductile deformation behaviour can be seen at the 100 nm thick Cu film on PI. Films with thicknesses less than 100 nm behave brittle and crack with increasing strain. Cu films above 100 nm film thickness show a ductile deformation behaviour by forming necks.

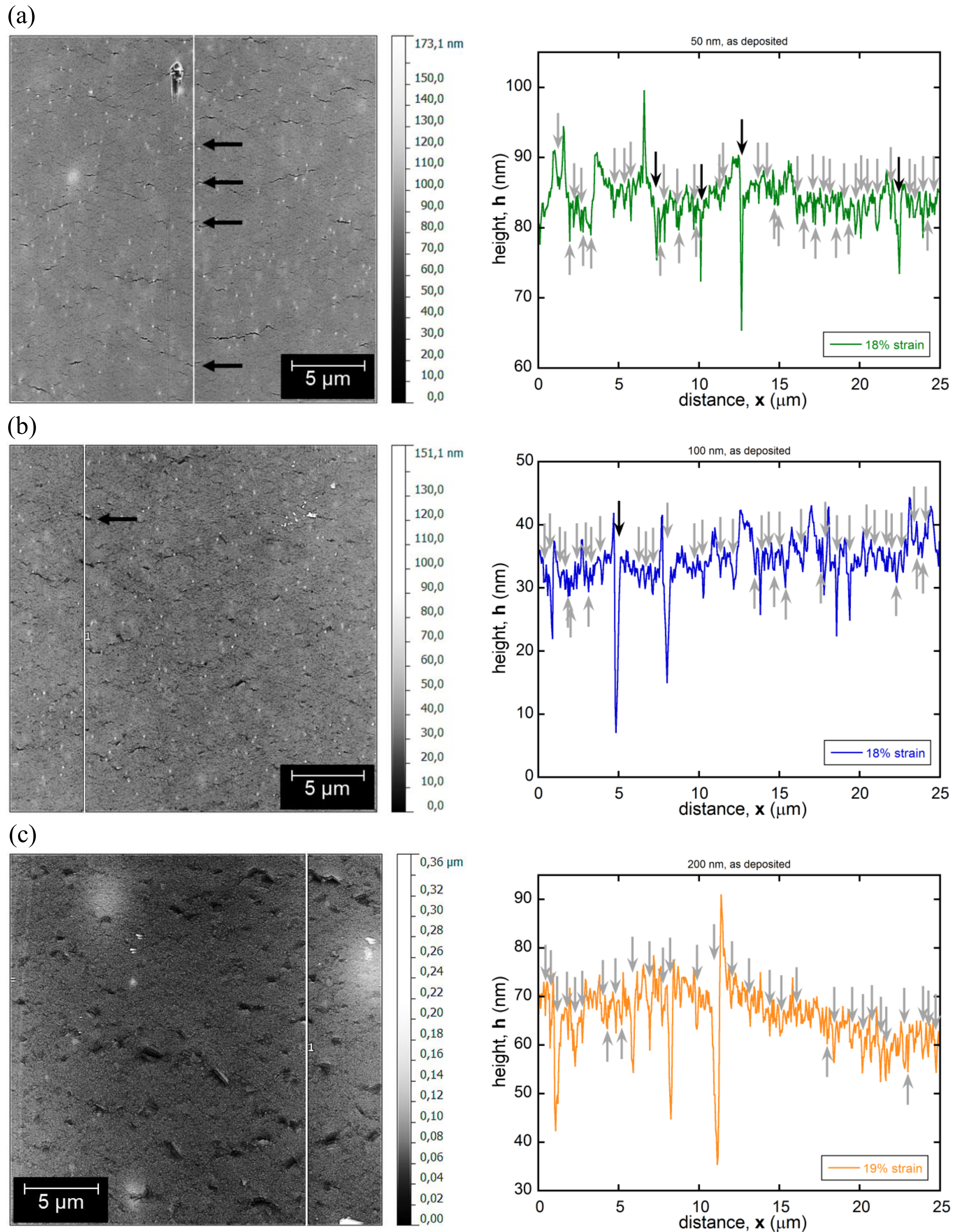

Fig. 5.1. *AFM height images with surface profiles of strained Cu films with different thicknesses. (a) 50 nm, 18% strained, (b) 100 nm, 18% strained and (c) 200 nm, 19% strained. Positions of channel cracks are indicated with black arrows and necks are marked with grey arrows. Note the different height scales used in the AFM images.*

Furthermore, looking at Fig. 5.2 it can be noted that plastic deformation (i. e. the formation of necks) occurs sooner in thicker films than in thinner films. For the 200 nm Cu film, necks start forming at ~ 2% strain, first signs of plastic deformation are visible in the 100 nm Cu film at about 3% strain and after approximately 6% strain, the 50 nm Cu film also started necking. The thicker films may neck earlier because of the presence of large-µm grains.

At about 15% strain, the deformation spacing remains roughly constant for all three Cu films with ~ 1 µm for the 200 nm film, ~ 0.5 µm for the 100 nm film and ~ 0.7 µm for the 50 nm film.

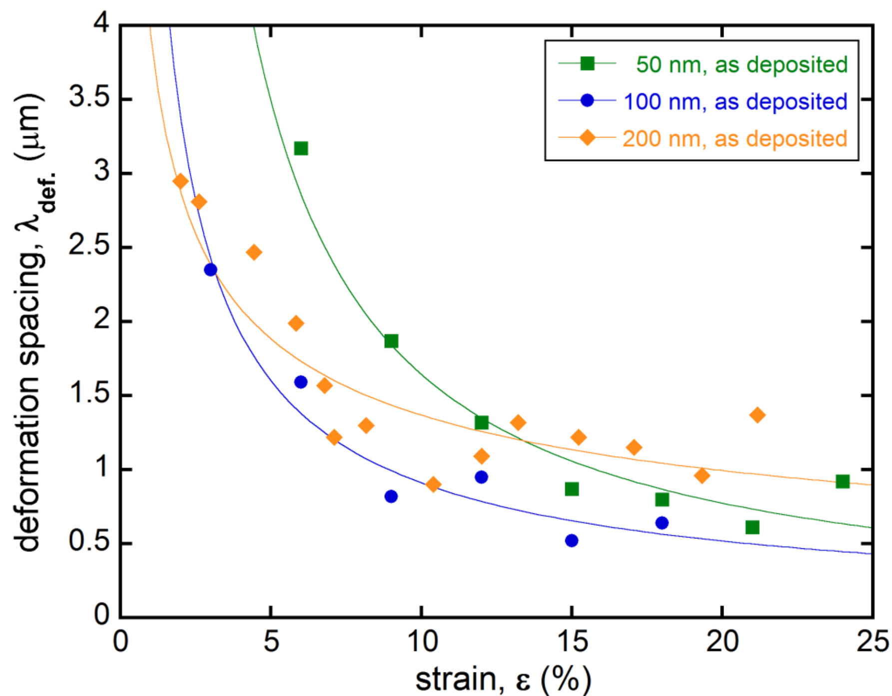

Fig. 5.2. Deformation spacing as a function of strain for as-deposited Cu-films with different film thicknesses. Each point in the graph is determined as the average value of three profiles over an AFM height image.

5.2 Effect of microstructure

In addition to the fragmentation tests of as-deposited Cu films (as discussed in section 5.1), the in-situ tensile test under the AFM has also been performed for an annealed 200 nm Cu film. AFM height images with the corresponding surface profiles are depicted in Fig. 5.3 for both as-deposited and annealed 200 nm Cu films. Comparing these images, it is evident that after 15% strain the annealed film exhibits more plastic deformation than the as-deposited one. Nevertheless, neither film showed through thickness cracking. The results of this

experiment compared to a non-annealed film are shown in Fig. 5.4, where the deformation spacing is plotted as function of the strain. Plastic deformation starts slightly earlier for the annealed than for the as-deposited sample. The average deformation spacing at saturation stage is approximately 0.8 µm for the annealed specimen and 1 µm for the as-deposited.

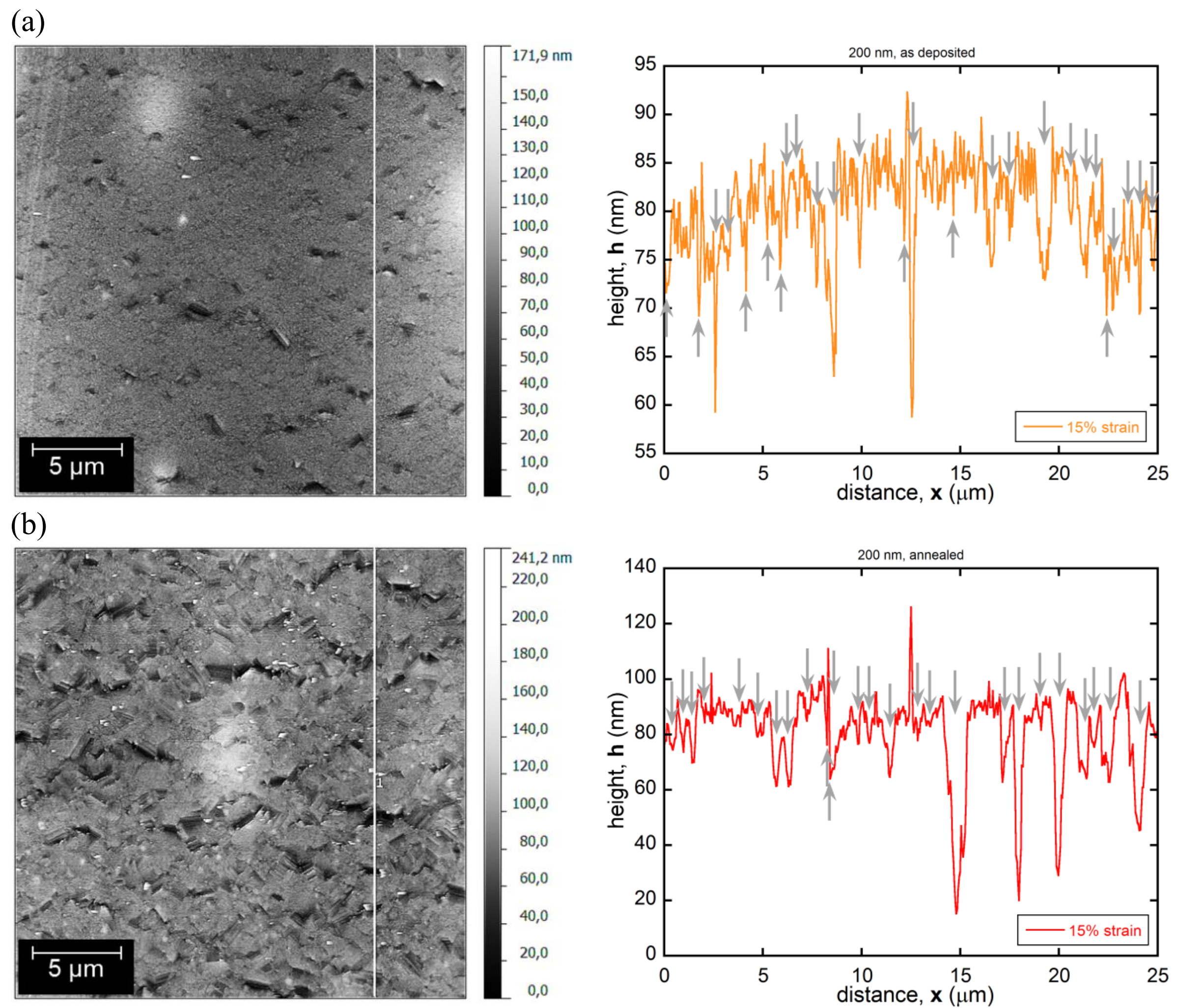

Fig. 5.3. *AFM height images with surface profiles of (a) an annealed (200 °C for 1 hour) and (b) an as-deposited 200 nm thick Cu film strained for 15%. Note the different height scales used in the AFM images. Grey arrows in the surface profiles indicate the positions, where necks have formed in the AFM image.*

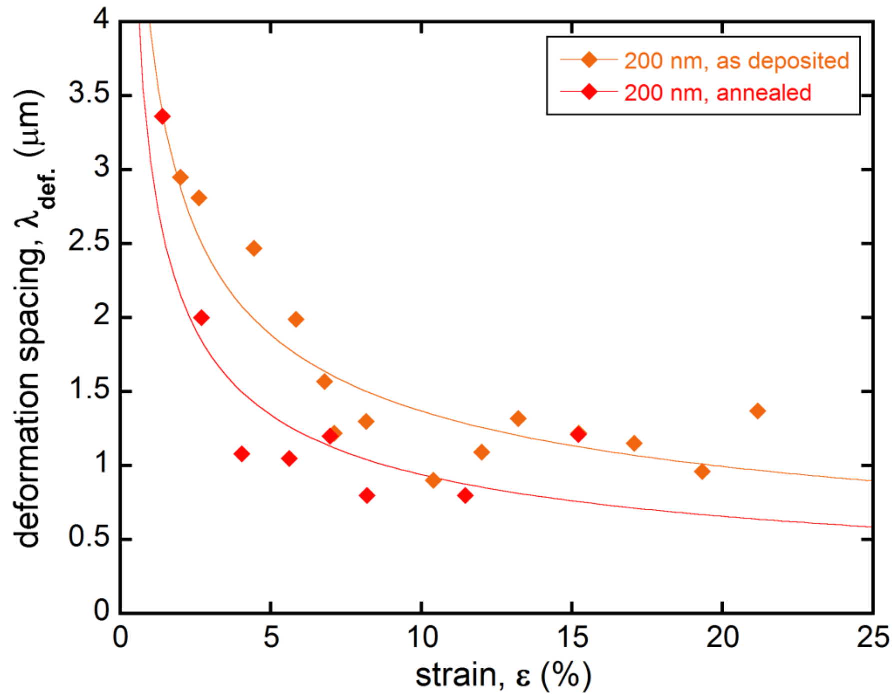

Fig. 5.4. *Deformation spacing as a function of strain for an as-deposited and an annealed Cu film.*

5.3 Drawbacks of the AFM fragmentation test method

AFM fragmentation testing does have a few disadvantages. First of all, each image takes at least 10 minutes to collect and finding the same spot for imaging is difficult. The data analysis is extremely time-consuming as well, and due to the limited resolution of the AFM height images, it is hard to distinguish between necks and surface roughness. Therefore a surface criteria ($\Delta/h < 2\%$) has been additionally established.

Secondly, imaging is complicated by the presence of surface inhomogeneities, which, however, make finding the same surface spot far easier. Because of these surface features the AFM tip may lose contact to the sample's surface and scanning artefacts arise. Therefore, it is of prime importance to use a low scanning speed and a sufficient scanning force. Another aberration may be caused by drift. To avoid drift, a waiting period of a couple of minutes between localizing the right spot and scanning is required. However, this cannot be realized for this thesis in order to limit the relaxation of the polymer substrate.

As a last point, due to the fact that Cu films deform plastically, the deformation does not have to occur perpendicular to the film surface. Cracks can form at every angle to the surface (Fig. 5.5) and can therefore not be detected satisfactory with the AFM tip. Moreover, the polymer substrate relaxes during imaging. Both, the non-adequate AFM imaging and the

substrate relaxation, lead to an underestimation of the deformation and crack density determined by AFM fragmentation tests.

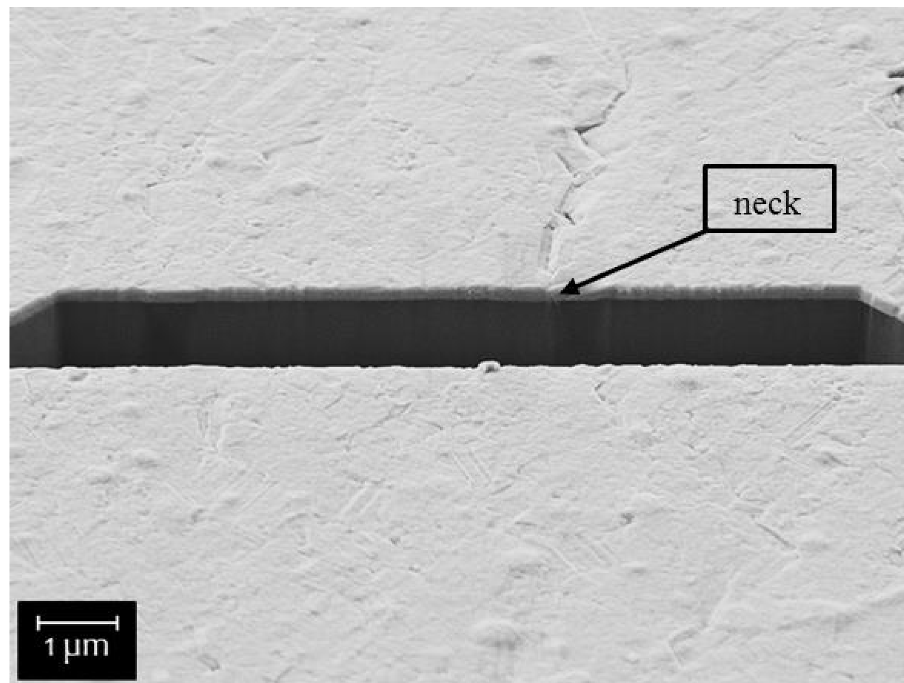

Fig. 5.5. *FIB cross-section of a neck in the 200 nm annealed Cu film after 20% strain. The neck formed at an angle to the surface. Image taken by R. Treml.*

5.4 Summary

In-situ fragmentation tests under the AFM have been performed in order to characterize the surface deformation of Cu films on PI depending on film thickness and microstructure. Film thickness was seen to have a greater effect on the mechanical deformation behaviour, rather than the as-deposited microstructure of the films. At the observed surface spots, 50 nm thick films showed both, necking and cracking, as a result of strain. For the 100 nm thick films, mainly necks and single TTCs were detected, while both the as-deposited and the annealed 200 nm thick films just thinned locally after straining the film for 24%. Plastic deformation occurred earlier in thicker films than in thinner films. Annealing of the 200 nm film just led to a slightly earlier start of neck formation. At approximately 15% strain, the deformation spacing remained constant for all four film systems ranging from 0.5 µm to 1 µm. Thus, it can be said, that Cu films with thicknesses less than 100 nm behave rather brittle and crack with increasing strain. Cu films above 100 nm film thickness show a ductile deformation behaviour by forming necks, which might be dominated by the present µm- large grains.

6 In-situ resistance measurements

6.1 Determination of R_{const}

As described in the experimental part (3.4), the measured resistance during straining, R_{meas}, has to be corrected by the constant remaining resistance under the grips, R_{const}, according to Equation 8. Table 6.1 shows the disparity between the actual resistance of the sample, R_{0samp} (externally measured by the device pictured in Fig. 3.6) and the measured initial resistance of the sample, R_{0meas}, where the sample is already mounted in the straining device (Fig. 3.5), expressed as R_{const}. Each value is averaged out of four different experiments per film system. Taking a more precise look at these data, it is obvious that R_{const} increases with decreasing film thickness. Moreover, there is hardly any difference in the resistance values between the annealed and the as-deposited 200 nm thick Cu film.

Tab. 6.1. *Electrical resistance values averaged out of four experiments per film system with their averaged deviations (av. dev.). R_{0samp} has been exhibited according to Fig. 3.6, R_{0meas} is measured as shown in Fig. 3.5 and R_{const} is calculated with Equation 9.*

film thickness (nm)		R_{0samp} (Ω)	av. dev. (Ω)	R_{0meas} (Ω)	av. dev. (Ω)	R_{const} (Ω)	av. dev. (Ω)
200	ann.	0.380	0.032	0.477	0.013	0.097	0.038
200	as dep.	0.419	0.022	0.510	0.027	0.091	0.039
100	as dep.	1.048	0.031	1.290	0.068	0.242	0.096
50	as dep.	3.777	0.217	4.307	0.212	0.530	0.005

6.2 Effect of film thickness

The change of the relative resistance, R/R_0, as a function of the relative elongation, L/L_0, is plotted in Fig. 5.1 for the tested as-deposited Cu films. The curves represent the mean relative resistance averaged from four experiments all strained up to 20%. The dotted line in the graph, labeled as 'theory', describes the constant volume assumption of Equation 8. As depicted in Fig. 6.1, the growth of the resistance of all strained films follows the theoretical line in the beginning. At approximately 6% strain, the relative resistance of the 50 nm thick Cu films starts to deviate from this trend-line. At this point, cracks start forming in the film. With increasing strain, the relative resistance of the 50 nm films deviates more and more from the theoretical prediction reaching its peak value, R_{max}, at the maximum strain. The fast increase of the resistance can be attributed to the lack of ductility due to the nanometer sized

grains. The 100 nm thick Cu films deviate considerably later at a failure strain of about 15% and there is no serious degradation of the electrical conductivity at the maximum strain of 20%. The 200 nm thick films, however, nearly behave like the theoretical line, which implies that there are no large structural changes in the film. Thus, Cu films above 100 nm film thickness show a ductile deformation behaviour, due to their homogenous microstructure in the µm-regime, which prohibits localized damage.

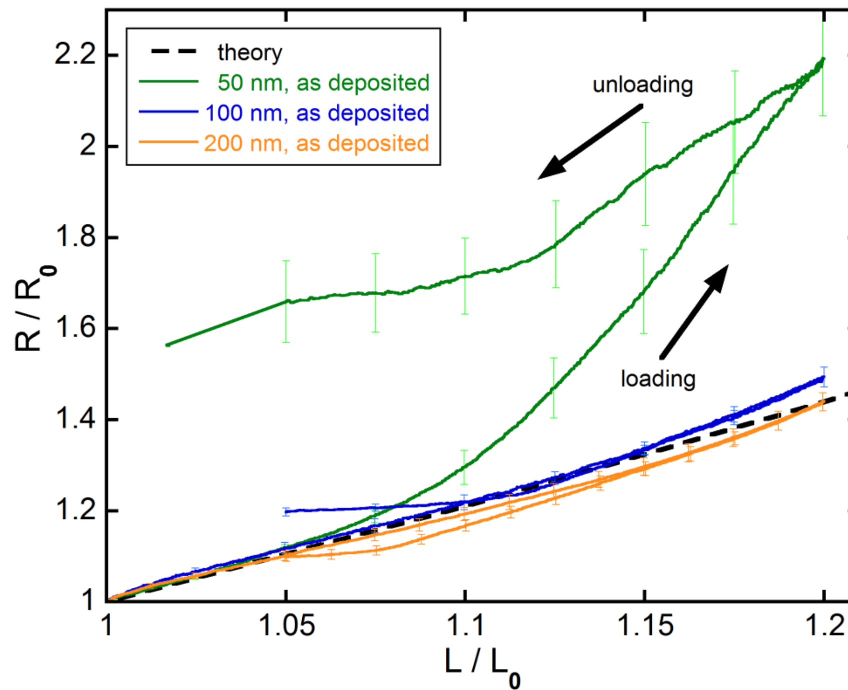

Fig. 6.1. *Change of the normalized electrical resistance, R/R_0, with increasing normalized length, L/L_0, during straining of as-deposited Cu films with different film thicknesses. The dotted line describes the constant volume assumption of Equation 8. Additionally to the loading curve (starting point (1,1)), also the unloading curve can be seen. The final resistance after fully unloading is noticeable higher than the initial resistance.*

When the maximum strain of 20% is reached, the films were unloaded until the samples were fully buckled between the grips. During unloading a decrease of resistance is observed. It is evident from Fig. 6.1 that the relative resistance does not totally recover, although there is no force on the sample anymore. The final resistance, R_f, of the unloaded, yet still mounted, samples is increased by approximately 10%, 20% and 66% for a 200 nm, a 100 nm and a 50 nm film, respectively. The average values of the initial resistances, the resistances at maximum strain and after relaxation as well as their relative values are summarized in Tab. 6.2 for as-deposited Cu films with different film thicknesses. Moreover,

the average failure strains (i.e. the strain, where the relative resistance curve starts to deviate from the theoretical line) for the 50 nm and the 100 nm thick Cu films are also listed in Tab. 6.2.

Tab. 6.2. *Average resistance values before straining (R_0), at maximum strain (R_{max}) and after unloading (R_f) for Cu films with different film thicknesses. Relative resistances at 20% strain (R_{max}/R_o) and after relaxation (R_f/R_0) are also listed for better comparability. If existing, failure strains ($\varepsilon_{failure}$) are stated too.*

film thickness (nm)	av. $\varepsilon_{failure}$ (%)	av. R_0 (Ω)	av. R_{max} (Ω)	av. R_f (Ω)
200	-	0.4192	0.6041	0.4603
100	15	1.0482	1.5671	1.2551
50	6	3.7771	8.3159	6.2868
film thickness (nm)	**av. R_{max}/R_0 (-)**	**av. dev. (-)**	**av. R_f/R_0 (-)**	**av. dev. (-)**
200	1.44	0.02	1.10	0.01
100	1.50	0.02	1.20	0.01
50	2.20	0.13	1.66	0.09

6.3 Effect of microstructure

Despite the obvious difference in the microstructure between the annealed and the as-deposited 200 nm Cu film (as described in Chapter 4 and depicted in Fig. 6.2), there is hardly any difference in their electro-mechanical behaviour (Fig. 6.3). This could be due to the fact that both contain large 1 µm grains, which could be dominating the behaviour. With increasing elongation of the sample the relative resistance of both curves rises constantly following the theoretical trend-line. The slope of the annealed curve is just slightly higher than the as-deposited curve. Due to the fact that none of the curves deviate from the constant volume assumption, cracking of the films is not expected. Via post-mortem SEM studies of the strained surfaces (Fig. 6.2), this behaviour could be confirmed; neither film showed through thickness cracking, but only necking. The maximal applied strain of 20% is below the failure strain and no cracks occur. At the maximum strain, the averaged electrical resistance, R_{max}, is 44% higher for the as-deposited samples and 51% higher for the annealed specimens than the average initial resistance.

During unloading, a decrease of resistance is observed. It is evident from Fig. 6.3 that at the beginning of unloading the relative resistance follows exactly its loading line for both samples. The annealed film does not show a fully recovery of the resistance either, as it has been discussed in section 6.2 for the as-deposited films. For the 200 nm thick Cu film the

average final resistance of the samples, R_f, is about 10% higher than the initial resistance, R_0, and for the annealed film, it is even 15% higher. All relevant averaged resistance values are summarized in Tab. 6.3 for the 200 nm thick Cu films with different surface modification.

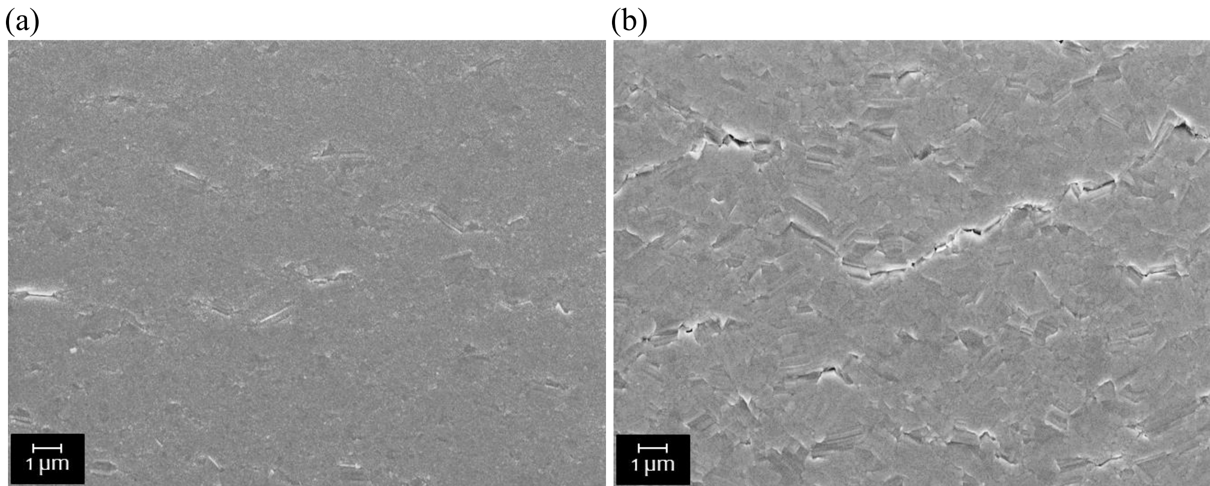

Fig. 6.2. *Post mortem SEM images of 200 nm thick Cu films on PI strained up to 20% with the 4PP straining device. (a) As-deposited film and (b) annealed film.*

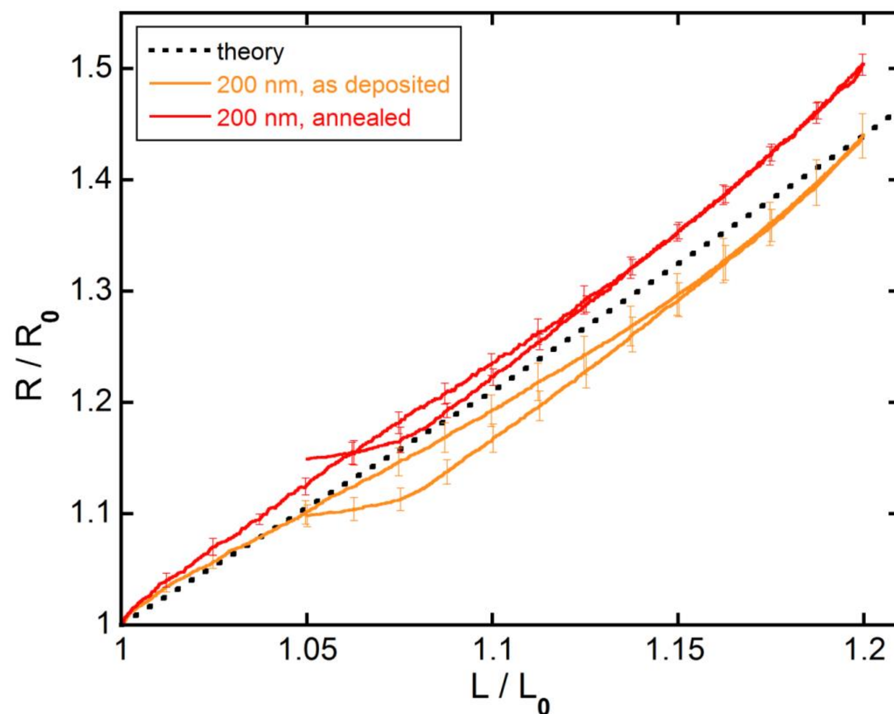

Fig. 6.3. *Change of the relative resistance, R/R_0, with increasing relative length, L/L_0, of as-deposited and annealed 200 nm thick Cu-films. The dotted line describes the constant volume assumption of Equation 8.*

Tab. 6.3. *Average (av.) resistance values before straining (R_0), at maximum strain (R_{max}) and after unloading (R_f) for as-deposited and annealed 200 nm thick Cu films. Relative resistances at 20% strain (R_{max}/R_o) and after relaxation (R_f/R_0) are listed for better comparability.*

200 nm Cu on PI	av. R_0 (Ω)	av. R_{max} (Ω)	R_{max}/R_0 (-)	av. dev. (-)	av. R_f (Ω)	R_f/R_0 (-)	av. dev. (-)
annealed	0.3795	0.5712	1.51	0.01	0.4366	1.15	0.01
as de-posited	0.4192	0.6041	1.44	0.02	0.4603	1.10	0.01

6.4 Summary

With the aid of in-situ resistance measurements during straining, mechanical damage induced in the film due to straining can be detected. With the initial formation in the film's cross-section, the electrical resistance of the film increases compared to its initial defect-free state. Therefore, measuring the alteration of the resistance of Cu films with different film thicknesses and microstructures has served as a way to determine the presence of cracks.

In the beginning, the film's elecrtical data (R/R_0) do not vary much from the theoretical behaviour and follow the constant volume assumption of Equation 8. The relative resistance of the 50 nm thick films starts deviating from the theoretical line much earlier (at ~ 6% strain) and stronger, than the relative resistance of the 100 nm thick films. Due to the increasing deviation of the former from the theoretical line, the crack density seems to rise severely with strain, which has already been proved by in-situ fragmentation tests under the AFM. For the 100 nm thick films, however, there is no serious degradation of the electrical conductivity ($R_{max}/R_0 = 1.5$) at the maximum strain of 20% as detected for the 50 nm samples ($R_{max}/R_0 = 2.2$). Thus, although cracks start forming at approximately 15% strain in the 100 nm thick films, their number hardly increases with further straining up to 20%. On the contrary, the 200 nm films, both as-deposited and annealed, follow the theorethical line well up to 20% strain without deviating and therefore without forming TTCs at all. Hence, the film thickness and not the film microstructure is the dominating feature in the deformation behaviour of Cu films on PI, because the as-deposited and annealed 200 nm film behave so similarly. Cu films with a film thickness under 100 nm show a brittle deformation behaviour by forming cracks; above 100 nm film thickness, a ductile deformation behaviour is present, most likely caused by the large grains in the µm-range.

7 Conclusion

Cu films with varying film thickness and grain size were studied using in-situ fragmentation testing, electrically via 4PP resistance measurements and mechanically with tensile tests under the AFM. For a better comparison between the fragmentation testing under the AFM and with 4PP resistance measurements, the results of both experiments were plotted separately for the different film thicknesses (Fig. 7.1 to Fig 7.3).

As a consequence of straining, the films deform plastically by forming necks. Plastic deformation occurs earlier in thicker films than in thinner ones. Moreover, necks form slightly earlier in the annealed 200 nm thick Cu film than in the as-deposited film. The neck density increases with strain and some of the necks even grow in depth. However, only for the 50 nm thick Cu film a transformation from necks to cracks is observed. At approximately 15% strain, the deformation spacing remains constant for all four film systems, when no further necks form with increasing strain.

The 50 nm film clearly isolates itself from the thicker films concerning deformation behaviour due to the formation of cracks, as shown in Fig. 7.1. At approximately 6% strain, when first necks are detected with the AFM, the relative resistance starts deviating from the theoretical prediction with constant volume assumption. With increasing strain, the resistance rises and the deformation spacing reaches a saturation level. At about 12% strain, when the slope in the relative resistance curve reaches a constant value, cracks appear on the surface and can be seen in AFM images. Thus, 50 nm thick Cu films on PI behave brittle and crack with increasing strain. Microstructural investigations show that the 50 nm thick films mainly consist of nano-sized grains with an average grain size of 38.5 nm, attributing the brittle deformation to the small grains.

For the 100 nm thick Cu films, the deviation of the relative resistance from the theoretical line initiated at about 15% strain, when the deformation spacing reaches an approximate constant value of 0.5 µm (Fig. 7.2). There is no serious degradation of the electrical conductivity at the maximum strain of 20% as detected for the 50 nm samples. Thus, the 100 nm films seem to behave in a ductile manner although consisting of nano-sized grains in the range of the film thickness. However, single through thickness cracks are observed at AFM and SEM micrographs at higher strains, which leads to the assumption that a brittle to ductile transition exists at film thicknesses of about 100 nm.

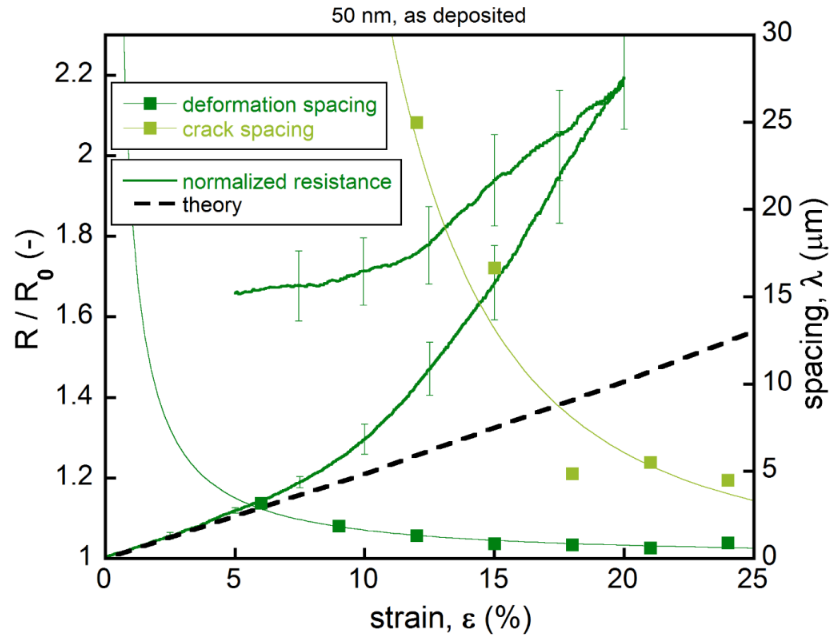

Fig. 7.1. Electrical and mechanical deformation behaviour as a function of strain for as-deposited 50 nm thick Cu films on PI. The dotted line describes the constant volume assumption of Equation 8. With beginning of neck formation at ~ 6% strain, the relative resistance starts deviating from the theoretical prediction. At ~ 12% strain, when the slope in the relative resistance curve reaches a constant value, cracks appear. Due to the strong deviation from the theoretical trend-line and the formation of cracks, 50 nm Cu films clearly show a brittle deformation behaviour.

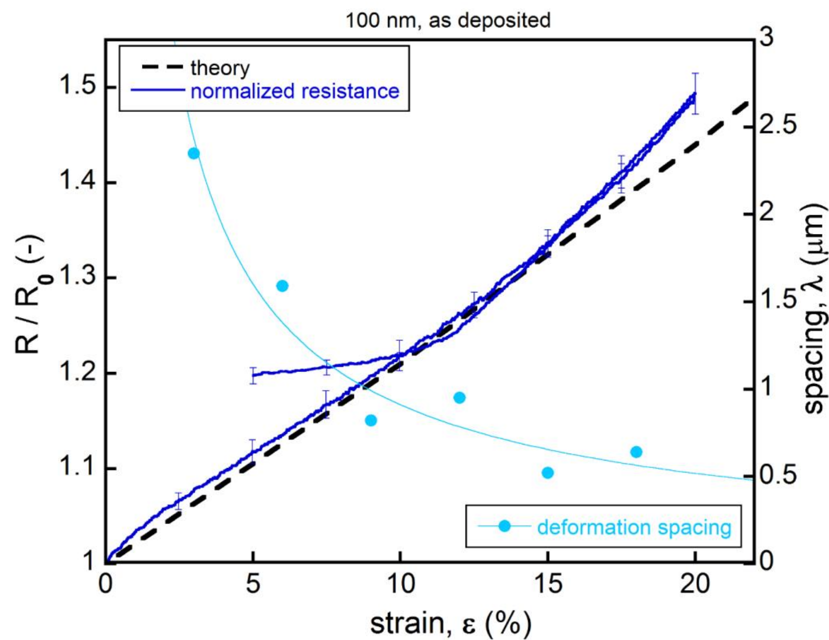

Fig. 7.2. Change of the relative resistance and the deformation spacing with increasing strain for as-deposited 100 nm thick Cu films on PI. When the relative resistance starts deviating from the theoretical line at ~ 15% strain, the deformation spacing remains constant.

The 200 nm films behave in a completely ductile manner. Both film's electrical data (R/R_0) do not vary much from the theoretical behaviour and follow the theorethical line well up to about 20% strain. At low strains, necking occurrs, which did not effect the electrictal resistance. Even when the deforamtion spacing reaches a saturation regime at approximately 10% strain, the electrical resistance is not greatly effected. Clearly the film thickness and not the film microstructure is the dominating feature in the deformation behaviour, because the two films (as-deposited and annealed) behave so similarly. As-deposited films show a bimodal microstructure with a few µm-large grains randomly distributed in a majority of nano-sized grains. With annealing, the percentage of the µm-sized grains rises. Therefore, the ductile deformation behaviour of the two films was most likely dominated by large µm scaled grains.

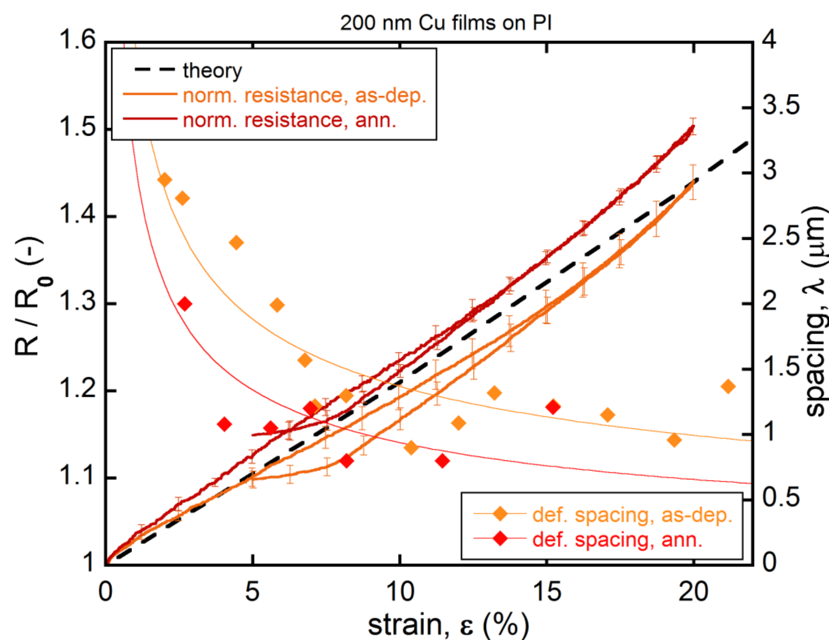

Fig. 7.3. *Electrical and mechanical deformation behaviour as a function of strain for 200 nm thick Cu films on PI with different microstructure. Both films behave in a completely ductile manner. Their electrical data (R/R_0) do not vary much from the theoretical behaviour and follow the theorethical line well up to 20% strain. Moreover, only necks are formed in the film during straining. The samples reach a saturation spacing of ~ 0.8 µm (annealed sample) and ~ 1 µm (as-deposited film) after approximately 10% strain.*

List of abbreviations

4PP	4 point probe
A_0, A	(initial) cross section of the film
ann.	annealed
as.-dep.	as-deposited
AFM	atomic force microscope
av.	average
av. dev.	average deviation
d	average grain size
E	elastic (Young's) modulus of the film
EBSD	electron back scatter diffraction
FIB	focused ion beam
h	film thickness
L/L_0	normalized length or relative elongation
L_0, L	(initial) gauge length (i.e. (initial) distance between the resistance measuring contacts)
ΔL	length variation due to straining
$l_{profile}$	length of the surface profile across an AFM or SEM micrograph
N_{cracks}	number of cracks
OM	optical microscope
PET	polyethylene terephthalate
PI	polyimide
R/R_0	normalized/relative resistance of the film
R_0, R	(initial) resistance of the film

R_{0meas}, R_{meas}	measured (initial) resistance of the film in the straining device falsified by R_{const}
R_{0samp}, R_{samp}	(initial) resistance of the sample restricted to the strained area of the film
R_{samp} / R_{0samp}	relative resistance of the strained sample
R_{const}	contact resistance (i.e. resistance of the film under the grips of the straining device)
R_f	final resistance of the strained film after unloading
R_{max}	maximum resistance of the strained film
sat.	saturation
SEM	scanning electron microscope
TEM	transmission electron microscope
TTCs	through thickness cracks
x	Position of deformation sites (necks or cracks) in horizontal direction
Δ	average deformation (neck or crack) depth
Δ/h	average depth value normalized to the film thickness
ε	engineering strain
ε_f	fracture/failure strain (i.e. strain, where first cracks appear)
λ	spacing
λ_{crack}	crack spacing (i.e. average distance between two cracks)
$\lambda_{sat.(crack)}$	crack spacing at saturation (i.e. crack spacing reaches a minimum and stays constant)
$\lambda_{def.}$	deformation spacing (i.e. average distance between two deformation sites (both necks and cracks))
λ_{max}	maximum fracture length
λ_{min}	minimum fracture length
$\lambda_{sat.(def.)}$	deformation spacing at saturation stage (i.e deformation spacing reaches a minimum and stays constant)

ρ	resistivity
ρ_{crack}	crack density
σ_f	fracture stress of the film
τ_{IFSS}	interfacial shear stress (i.e. maximum shear stress sustained at the film-substrate interface)

List of figures

Fig. 2.1. (a) Average (ave.) crack spacing as a function of strain of a 50 nm Cu/Cr film determined with the aid of AFM micrographs compared to the crack evolution established by SEM micrographs. (b) SEM micrograph at 20% strain of the 50 nm Cu/Cr film illustrating the brittle crack formation. (c) Change of the deformation spacing with increasing strain for a 200 nm Cu/Cr film. In contrast to (a), the deformation spacings determined with AFM and SEM micrographs have different values. This is because of the difficulty to accurately measure the TTC and neck spacings in SEM micrographs for ductile films, as demonstrated in (d) for a 15% strained, 200 nm Cu/Cr film. After a certain amount of strain, both films reach saturation in crack spacing (a) and deformation spacing (c), where no further cracks and necks form. This saturation is indicated by the plateau [8]. **5**

Fig. 2.2. AFM height images at (a) 2%, (b) 8% and (c) 15% strain of a 200 nm Cu/Cr/PI-system. In (d) the corresponding surface profiles from (a), (b) and (c) are shown and it is indicated where necks and TTCs have formed. Grey arrows represent necks and black arrows TCCs [8]. **6**

Fig. 2.3. Change of the relative resistance with increasing relative length of the strained sample during loading and unloading. The short dotted and the solid curve show the difference between measured (R_{meas}/R_{0meas}) and the corrected (R_{samp}/R_{0samp}) relative resistances. The dashed line, labelled as Eq. (4) corresponds to the constant volume assumption of Equation 8. Eq. (3) can be neglected [16]. **9**

Fig. 2.4. Schematic diagram of the brittle failure behaviour of thin metal films showing both failure stress and shear stress as function of the distance between two cracks. (b) If $\lambda_{max} = 2\lambda_{min}$ no further fracture of the film happens [9]. **10**

Fig. 2.5. Schematic of the deformation behaviour of (a) a freestanding ductile thin metal film, (b) a brittle, substrate bonded metal film (c) a ductile thin metal film well bonded to a substrate and (d) a ductile thin metal film debonding from the substrate. **12**

Fig. 2.6. Schematic diagram of the microstructural changes in a Cu film on Kapton during straining. For forming a neck, three things coevolve: deformation-associated grain growth, strain localization promoted by large grains and the local delamination of the film from the substrate [14]. **13**

Fig. 2.7. Relative resistance, R/R_0, as a function of the relative length, L/L_0, for as-deposited and annealed Cu films compared to the constant volume assumption ($R/R_0 = (L/L_0)^2$) [14]. **14**

Fig. 2.8. Stress–strain curves of freestanding Cu films with variations in thickness before and after annealing. Differences in yield stress and transition from the elastic to the plastic deformation behaviour can be explained with the respective microstructure [37]. **15**

Fig. 2.9. Relative resistance, R/R_0, as a function of uniaxial film elongation for sputtered Cu foils on PI with variation in their film thicknesses. $R/R_0 = (L/L_0)^2$ describes the constant volume assumption [15]. **16**

Fig. 2.10. Change of the failure strain, ε_r, with increasing film thickness, h, due to different fracture behaviours [15]. **16**

Fig. 3.1. AFM images with surface profiles at (a) 6% strain, (b) 15% stain and (c) 24% strain of a 50 nm Cu film. Positions of channel cracks are indicated with black arrows. Note the different height scales used in the AFM images. **21**

Fig. 3.2. Surface profiles of the 50 nm Cu on PI from Fig. 3.1(a), (b) and (c) indicating where necks and TTCs have formed. Gray arrows represent necks and black arrows TTCs. **22**

Fig. 3.3. Segment of Fig. 3.2 expressing the difference between deformation spacing, λ_{def}, and crack spacing, λ_{crack}. The deformation spacing corresponds to the average distance between two deformation sites (necks and cracks), whereas the crack spacing just defines the average distance between two cracks. **22**

Fig. 3.4. Evolution of crack and deformation density as a function of strain for the in Fig. 3.1 shown AFM experiment of a 50 nm Cu film. Necks arise at about 6% strain and cracks start forming at approximately 12% strain. The fitted line through the data points is just to guide the eye. **23**

Fig. 3.5. Schematic diagram of the used 4PP resistance measurement setup. For clear understanding, the probing contacts were plotted further apart. Meanwhile, they are positioned at the inner edge of the grips. Thus, L_{const} can be assumed as zero and the distance between the probing contacts equals the gauge length. The initial gauge length, $L_{0,}$ is 20 mm. The inset photo shows a mounted sample between the grips of the straining device [16]. **24**

Fig. 3.6. (a) Schematic and (b) photo of the 4PP resistance measurement setup for determining R_{0samp}. **25**

Fig. 4.1. Grain size histograms of 20% strained, as-deposited 50 nm and 100 nm thick Cu films. Grain sizes were characterized at plan view TEM micrographs. **26**

Fig. 4.2. Column diagrams showing the different trend in grain size distribution between as-deposited and annealed 200 nm Cu films, both strained to 21%. Grain sizes were determined by the EBSD software TSL OIM Analysis version 5.31. **27**

Fig. 4.3. Plan view TEM micrographs of (a) a 50 nm and (b) a 100 nm thick Cu film. Images taken by V. Maier. **28**

Fig. 4.4. Ion channelling contrast images of (a) the as-deposited and (b) the annealed 200 nm thick Cu film, illustrating the bimodal grain size of the as-deposited compared to the more homogeneous grains of the annealed film. Taken by (a) B. Völker and (b) R. Treml. **28**

Fig. 4.5. EBSD orientation maps of 200 nm thick Cu films (a) without and (b) with heat treatment (200° C, 1 h) strained to 21%. The orientation of the grains is represented with the help of the orientation colour key (c). The confidence index was set to be 0.05; all grains not meeting this criterion are coloured black in the scan. Relatively random grain alignment with slightly more (111) and (100) orientated grains for both films, the as-deposited (d) and the annealed film (e). **29**

Fig. 4.6. EBSD orientation maps of an annealed 200 nm Cu film showing the same spot for (a) 0% strain, (b) 5% strain and (c) 10% strain. **30**

Fig. 5.1. AFM height images with surface profiles of strained Cu films with different thicknesses. (a) 50 nm, 18% strained, (b) 100 nm, 18% strained and (c) 200 nm, 19% strained. Positions of channel cracks are indicated with black arrows and necks are marked with grey arrows. Note the different height scales used in the AFM images. **33**

Fig. 5.2. Deformation spacing as a function of strain for as-deposited Cu-films with different film thicknesses. Each point in the graph is determined as the average value of three profiles over an AFM height image. **34**

Fig. 5.3. AFM height images with surface profiles of (a) an annealed (200 °C for 1 hour) and (b) an as-deposited 200 nm thick Cu film strained for 15%. Note the different height scales used in the AFM images. Grey arrows in the surface profiles indicate the positions, where necks have formed in the AFM image. **35**

Fig. 5.4. Deformation spacing as a function of strain for an as-deposited and an annealed Cu film. **36**

Fig. 5.5. FIB cross-section of a neck in the 200 nm annealed Cu film after 20% strain. The neck formed at an angle to the surface. Image taken by R. Treml. **37**

Fig. 6.1. Change of the normalized electrical resistance, R/R_0, with increasing normalized length, L/L_0, during straining of as-deposited Cu films with different film thicknesses. The dotted line describes the constant volume assumption of Equation 8. Additionally to the loading curve (starting point (1,1)), also the unloading curve can be seen. The final resistance after fully unloading is noticeable higher than the initial resistance. **39**

Fig. 6.2. Post mortem SEM images of 200 nm thick Cu films on PI strained up to 20% with the 4PP straining device. (a) As-deposited film and (b) annealed film. **41**

Fig. 6.3. Change of the relative resistance, R/R_0, with increasing relative length, L/L_0, of as-deposited and annealed 200 nm thick Cu-films. The dotted line describes the constant volume assumption of Equation 8. **41**

Fig. 7.1. Electrical and mechanical deformation behaviour as a function of strain for as-deposited 50 nm thick Cu films on PI. The dotted line describes the constant volume assumption of Equation 8. With beginning of neck formation at ~ 6% strain, the relative resistance starts deviating from the theoretical prediction. At ~ 12% strain, when the slope in the relative resistance curve reaches a constant value, cracks appear. Due to the strong deviation from the theoretical trend-line and the formation of cracks, 50 nm Cu films clearly show a brittle deformation behaviour. **44**

Fig. 7.2. Change of the relative resistance and the deformation spacing with increasing strain for as-deposited 100 nm thick Cu films on PI. When the relative resistance starts deviating from the theoretical line at ~ 15% strain, the deformation spacing remains constant. **44**

Fig. 7.3. Electrical and mechanical deformation behaviour as a function of strain for 200 nm thick Cu films on PI with different microstructure. Both films behave in a completely ductile manner. Their electrical data (R/R_0) do not vary much from the theoretical behaviour and follow the theorethical line well up to 20% strain. Moreover, only necks are formed in the film during straining. The samples reach a saturation spacing of ~ 0.8 µm (annealed sample) and ~ 1 µm (as-deposited film) after approximately 10% strain. **45**

List of tables

Tab. 4.1. Average (av.) grain size and its standard deviation listed for as-deposited and annealed Cu films on polyimide. The standard deviations for the 200 nm thick films are huge due to their bimodal grain size. **27**

Tab. 4.2. Average (av.) grain size inclusive standard deviation for different straining steps of an as-deposited and an annealed 200 nm thick Cu film determined out of the in-situ EBSD data. The standard deviations are huge due to the bimodal grain size showing large-µm grains in a nano-sized matrix. **31**

Tab. 6.1. Electrical resistance values averaged out of four experiments per film system with their averaged deviations (av. dev.). R_{0samp} has been exhibited according to Fig. 3.6, R_{0meas} is measured as shown in Fig. 3.5 and R_{const} is calculated with Equation 9. **38**

Tab. 6.2. Average (av.) resistance values before straining (R_0), at maximum strain (R_{max}) and after unloading (R_f) for Cu films with different film thicknesses. Relative resistances at 20% strain (R_{max}/R_o) and after relaxation (R_f/R_0) are also listed for better comparability. If existing, failure strains ($\varepsilon_{failure}$) are stated too. **40**

Tab. 6.3. Average (av.) resistance values before straining (R_0), at maximum strain (R_{max}) and after unloading (R_f) for as-deposited and annealed 200 nm thick Cu films. Relative resistances at 20% strain (R_{max}/R_o) and after relaxation (R_f/R_0) are listed for better comparability. **42**

References

[1] M.J. Cordill, Flexible film systems: Current understanding and future prospects, JOM 62(6) (2010) 9-14.

[2] N. Lu, Mechanics of hard films on soft substrates, Dissertation, Harvard University (2009).

[3] A. Kelly, W.R. Tyson, Tensile properties of fiber reinforced metals: Copper/tungsten and copper/molybdenum, Journal of the Mechanics and Physics of Solids 13 (1965) 329-350.

[4] D.C Agrawal, R. Raj, Measurement of the ultimate shear strength of a metal-ceramic interface, Acta Metallurgica 37(4) (1989) 1265-1270.

[5] Y. Leterrier, L. Boogh, J. Andersons, J.-A.E. Månson, Adhesion of silicon oxide layers on poly (ethylene terephthalate). I: Effect of substrate properties on coating's fragmentation process, Journal of Polymer Science Part B: Polymer Physics 35 (1997) 1449–1461.

[6] M.S Hu, A.G. Evans, The cracking and decohesion of thin films on ductile substrates, Acta Metallurgica 37(3) (1989) 917-925.

[7] M.J. Cordill, V.M. Marx, In-situ tensile straining of metal films on polymer substrates under an AFM, Materials Research Society Symposium Proceedings 1527 (2013) mrsf12-1527-uu06-07.

[8] M.J. Cordill, V.M. Marx, Fragmentation testing for ductile thin films on polymer substrates, Philosophical Magazine Letters 93(11) (2013) 618–624.

[9] A.A. Taylor, V. Edlmayr, M.J. Cordill, G. Dehm, The effect of film thickness variations in periodic cracking: Analysis and experiments, Surface & Coatings Technology 206 (2011) 1830–1836.

[10] A.A. Taylor, M.J. Cordill, G. Dehm, On the limits of the interfacial yield model for fragmentation testing of brittle films on polymer substrates, Philosophical Magazine 92 (2012) 25-27.

[11] J. Andersons, S. Tarasovs, Y. Leterrier, Evaluation of thin film adhesion to a compliant substrate by the analysis of progressive buckling in the fragmentation test, Thin Solid Films 517 (2009) 2007–2011.

[12] M.J. Cordill, F.D. Fischer, F.G. Rammerstorfer, G. Dehm, Adhesion energies of Cr thin films on polyimide determined from buckling: Experiment and model, Acta Materialia 58 (2010) 5520–5531.

[13] O. Glushko, M.J. Cordill, Electrical resistance decrease due to grain coarsening under cyclic deformation, JOM 66(4) (2014) 598-601.

[14] N. Lu, X. Wang, Z. Suo, J. Vlassak, Failure by simultaneous grain growth, strain localization, and interface debonding in metal films on polymer substrates, Journal of Materials Research 24(2) (2009) 379-385.

[15] N. Lu, Z. Suo, J.J. Vlassak, The effect of film thickness on the failure strain of polymer-supported metal films, Acta Materialia 58 (2010) 1679–1687.

[16] O. Glushko, M.J. Cordill, Electrical resistance of metal films on polymer substrates under tension, Experimental Techniques (2014) in press.

[17] N. Lu, X. Wang, Z. Suo, J. Vlassak, Metal films on polymer substrates stretched beyond 50%, Applied Physics Letters 91 (2007) 221909-1-3.

[18] R.M. Niu, G. Liu, C. Wang, G. Zhang, X.D. Ding, J. Sun, Thickness dependent critical strain in submicron Cu films adherent to polymer substrate, Applied Physics Letters 90 (2007) 161907-1-3.

[19] F. Macionczyk, W. Brückner, Tensile testing of AlCu thin films on polyimide foils, Journal of Applied Physics 86(9) (1999) 4922-4929.

[20] M.M. Hamasha, K. Alzoubi, J.C. Switzer III, S. Lu, S.B. Desu, M. Poliks, A study on crack propagation and electrical resistance change of sputtered aluminium thin film on poly ethylene terephthalate substrate under stretching, Thin Solid Films 519(22) (2011) 7918-7924.

[21] B.E. Alaca, M.T.A. Saif, H. Sehitoglu, On the interface debond at the edge of a thin film on a thick substrate, Acta Materialia 50 (2002) 1197-1209.

[22] G.-D. Sim, S. Won, C.-Y. Jin, I. Park, S.B. Lee, J.J. Vlassak, Improving the stretchability of as-deposited Ag coatings on poly-ethylene-terephthalate substrates through use of an acrylic primer, Journal of Applied Physics 109 (2011) 073511-073515.

[23] O. Glushko, V.M. Marx, C. Kirchlechner, I. Zizak, M.J. Cordill, Recovery of electrical resistance in copper films on polyethylene terephthalate subjected to a tensile strain, Thin Solid Films 552 (2014) 141–145.

[24] W.A. Curtin, Exact theory of fibre fragmentation in a single-filament composite, Journal of Materials Science 26 (1991) 5239-5253.

[25] R.R. Keller, J.M. Phelps, D.T. Read, Tensile and fracture behavior of free-standing copper films, Materials Science and Engineering A214 (1996) 42–52.

[26] H. Huang, F. Spaepen, Tensile testing of free-standing Cu, Ag and Al thin films and Ag/Cu multilayers, Acta Materialia 48 (2000) 3261–3269.

[27] S.L. Chiu, J. Leu, P.S. Ho, Fracture of metal-polymer line structures. I. Semiflexible polyimide, Journal of Applied Physics 76(9) (1994) 5136–5142.

[28] M. Hommel, O. Kraft, Deformation behavior of thin copper films on deformable substrates, Acta Materialia 49 (2001) 3935–3947.

[29] D.Y.W. Yu, F. Spaepen, The yield strength of thin copper films on Kapton, Journal of Applied Physics 95 (2003) 2991–2997.

[30] S.P. Lacour, S. Wagner, Z. Huang, Z. Suo, Stretchable gold conductors on elastomeric substrates, Applied Physics Letters 82(15) (2003) 2404–2406.

[31] Y. Xiang, T. Li, Z. Suo, J.J. Vlassak, High ductility of a metal film adherent on a polymer substrate, Applied Physics Letters 87 (2005) 161910-1-3.

[32] T. Li, Z. Suo, Deformability of thin metal films on elastomer substrates, International Journal of Solids and Structures 43 (2006) 2351–2363.

[33] T. Li, Z. Suo, Ductility of thin metal films on polymer substrates modulated by interfacial adhesion, International Journal of Solids and Structures 44 (2007) 1696–1705.

[34] T. Li, Z.Y. Huang, Z.C. Xi, S.P. Lacour, S. Wagner, Z. Suo, Delocalizing strain in a thin metal film on a polymer substrate, Mechanics of Materials 37 (2005) 261–273.

[35] M.J. Cordill, A. Taylor, J. Schalko, G. Dehm, Microstructure and adhesion of as-deposited and annealed Cu/Ti films on polyimide, International Journal of Materials Research 102(6) (2011) 1-6.

[36] R.M. Niu, G. Liu, C. Wang, G. Zhang, X.D. Ding, J. Sun, Thickness dependent critical strain in submicron Cu films adherent to polymer substrate, Applied Physics Letters 90 (2007) 161907-1-3.

[37] Y. Xiang, T.Y. Tsui, J.J. Vlassak, The mechanical properties of freestanding electroplated Cu thin films, Journal of Materials Research 21(6) (2006) 1607-1618.

[38] Plano GmbH – Zubehör für Elekronenmikroskopie, http://www.cp-download.de/plano11/Kapitel-1.pdf (May 2014) 14.

[39] A.A. Taylor, M.J. Cordill, G. Moser, G. Dehm, A mechanical method for preparing TEM samples from brittle films on compliant substrates, Practical Metallography 48(8) (2011) 408-413.

[40] M.D. Abramoff, P.J. Magalhaes, S.J. Ram, Image processing with ImageJ, Biophotonics International 11(7) (2004) 36-42.

[41] D. Nečas, P. Klapetek, Gwyddion: an open-source software for SPM data analysis, Central European Journal of Physics 10(1) (2012) 181-188.